LETTER

doi:10.1038/nature13593

OSCA1 mediates osmotic-stress-evoked Ca^{2+} increases vital for osmosensing in *Arabidopsis*

Fang Yuan[1,2], Huimin Yang[1]*, Yan Xue[1]*, Dongdong Kong[1], Rui Ye[1], Chijun Li[1], Jingyuan Zhang[1,2], Lynn Theprungsirikul[1], Tayler Shrift[1], Bryan Krichilsky[1], Douglas M. Johnson[3], Gary B. Swift[3], Yikun He[1], James N. Siedow[1] & Zhen-Ming Pei[1]

Water is crucial to plant growth and development. Environmental water deficiency triggers an osmotic stress signalling cascade, which induces short-term cellular responses to reduce water loss and long-term responses to remodel the transcriptional network and physiological and developmental processes[1–4]. Several signalling components that have been identified by extensive genetic screens for altered sensitivities to osmotic stress seem to function downstream of the perception of osmotic stress. It is known that hyperosmolality and various other stimuli trigger increases in cytosolic free calcium concentration ($[Ca^{2+}]_i$)[5,6]. Considering that in bacteria and animals osmosensing Ca^{2+} channels serve as osmosensors[7,8], hyperosmolality-induced $[Ca^{2+}]_i$ increases have been widely speculated to be involved in osmosensing in plants[1,9]. However, the molecular nature of corresponding Ca^{2+} channels remain unclear[6,10,11]. Here we describe a hyperosmolality-gated calcium-permeable channel and its function in osmosensing in plants. Using calcium-imaging-based unbiased forward genetic screens we isolated *Arabidopsis* mutants that exhibit low hyperosmolality-induced $[Ca^{2+}]_i$ increases. These mutants were rescreened for their cellular, physiological and developmental responses to osmotic stress, and those with clear combined phenotypes were selected for further physical mapping. One of the mutants, *reduced hyperosmolality-induced $[Ca^{2+}]_i$ increase 1* (*osca1*), displays impaired osmotic Ca^{2+} signalling in guard cells and root cells, and attenuated water transpiration regulation and root growth in response to osmotic stress. OSCA1 is identified as a previously unknown plasma membrane protein and forms hyperosmolality-gated calcium-permeable channels, revealing that OSCA1 may be an osmosensor. OSCA1 represents a channel responsible for $[Ca^{2+}]_i$ increases induced by a stimulus in plants, opening up new avenues for studying Ca^{2+} machineries for other stimuli and providing potential molecular genetic targets for engineering drought-resistant crops.

The lack of information regarding the molecular nature of Ca^{2+} channels responsible for increases in $[Ca^{2+}]_i$ induced by various stimuli prompted us to design forward genetic screens to identify these sensory channels. With the assumption that osmosensing is the initial signalling event, the design was devised on the basis that the hyperosmolality-induced $[Ca^{2+}]_i$ increase (OICI) is the earliest detectable event (~5 s) upon hyperosmolality treatment (Extended Data Fig. 1a and Supplementary Information). Note that in contrast to traditional genetic screens, in which the phenotypes scored can take hours or days to reach a steady state, the entire transient OICI event lasts only ~5 min. The variation of the OICI could result in enormous numbers of false positives and make these screens difficult to apply, possibly explaining why for over 20 years the phenomena of stimulus-triggered $[Ca^{2+}]_i$ increases have only recently been dissected genetically[12,13] and the corresponding Ca^{2+} channels still remain unknown.

To optimize screening conditions for mutants with reduced OICI, we grew ethyl methane sulphonate-mutagenized aequorin-expressing *Arabidopsis* M2 seeds, treated these seedlings with several concentrations of sorbitol, and analysed aequorin luminescence for each seedling (Extended Data Fig. 1b). At 600 mM sorbitol, few seedlings had relative intensities lower than an arbitrary threshold, a noise level that was practical for use in genetic screens. We screened 85,600 M2 seeds, selected seedlings with low OICI signals (Extended Data Fig. 1c), tested these seedlings individually for four generations, and isolated 23 putative mutants with reduced OICI. Then, several criteria were used to rank these mutants for further physical mapping: there was no mutation in aequorin; the morphology of mutant plants was similar to that of wild type throughout developmental stages; the root growth response to osmotic stress was compromised; the stomatal response to osmotic stress was affected; and finally the phenotype of reduced OICI could be verified at the cellular level by using another Ca^{2+} indicator. After these rescreens and verifications, we named the most affected mutant as *reduced hyperosmolality-induced $[Ca^{2+}]_i$ increase 1* (*osca1*), and describe it here.

The basal $[Ca^{2+}]_i$ was similar in wild-type and *osca1* plants; while under sorbitol treatment $[Ca^{2+}]_i$ was much lower in *osca1* (Fig. 1a, b; $P < 0.001$). The reduced OICI was not due to a lesser amount of total aequorin (Extended Data Fig. 2a, b). We analysed the kinetics of the OICI using aequorin luminometry and observed that amplitudes were reduced in *osca1* mutants (Fig. 1c). Then, we determined the dose dependence of the OICI (Fig. 1d). A Hill curve could be fitted to the data with an apparent dissociation constant (K_d) of 698 ± 23 mM and 981 ± 69 mM for wild type and *osca1*, respectively. Hill coefficients were 3.8 and 2.0 for wild type and *osca1*, respectively. Seedlings were treated with solutions containing mannitol, sucrose, ribose or *N*-methyl-D-glucamine, and reduced OICIs were also recorded in *osca1* (Extended Data Fig. 2c). In addition, *osca1* roots were slightly less sensitive to sorbitol treatment (Extended Data Fig. 2d). The apparent K_d of wild-type and *osca1* plants were 382 ± 18 mM and 411 ± 21 mM, respectively. Furthermore, to determine if OSCA1 is specific to hyperosmolality over other stimuli, we analysed $[Ca^{2+}]_i$ elevation in response to H_2O_2, a well-documented inducer of increased $[Ca^{2+}]_i$ (refs 4, 6, 14), and observed no difference between wild type and *osca1* (Fig. 1e). These results demonstrated that $[Ca^{2+}]_i$ increases induced specifically by hyperosmolality are impaired in *osca1*, and that OSCA1 might be a major component of the OICI.

To rule out the possibility that the low OICI at the whole-plant level was caused by the inefficient detection of $[Ca^{2+}]_i$ by aequorin, we used another Ca^{2+} indicator, yellow Cameleon 3.6, that delivers a higher temporospatial resolution[14–16]. Note that we adopted several methods for analysing abscisic acid (ABA)-induced $[Ca^{2+}]_i$ increases in guard cells and stomatal closure[4,14,16,17]. Addition of sorbitol induced $[Ca^{2+}]_i$ increases in both wild-type and *osca1* guard cells; however, the amplitudes were significantly lower in *osca1* (Fig. 2a–c). Similar OICI defects were seen in *osca1* root cells (Extended Data Fig. 2e–g).

For a given sensor, after the conversion of the external signal into a secondary messenger, the signal should be funnelled on to downstream processes. We assessed whether OSCA1 is required for cellular processes that are known to be regulated by osmotic stress; that is, processes downstream of the sensor. Stomatal pores formed by pairs of guard cells are

[1]Department of Biology, Duke University, Durham, North Carolina 27708, USA. [2]Center on Plant Environmental Sensing, College of Life and Environmental Sciences, Hangzhou Normal University, Hangzhou, Zhejiang 310036, China. [3]Department of Physics, Duke University, Durham, North Carolina 27708, USA.
*These authors contributed equally to this work.

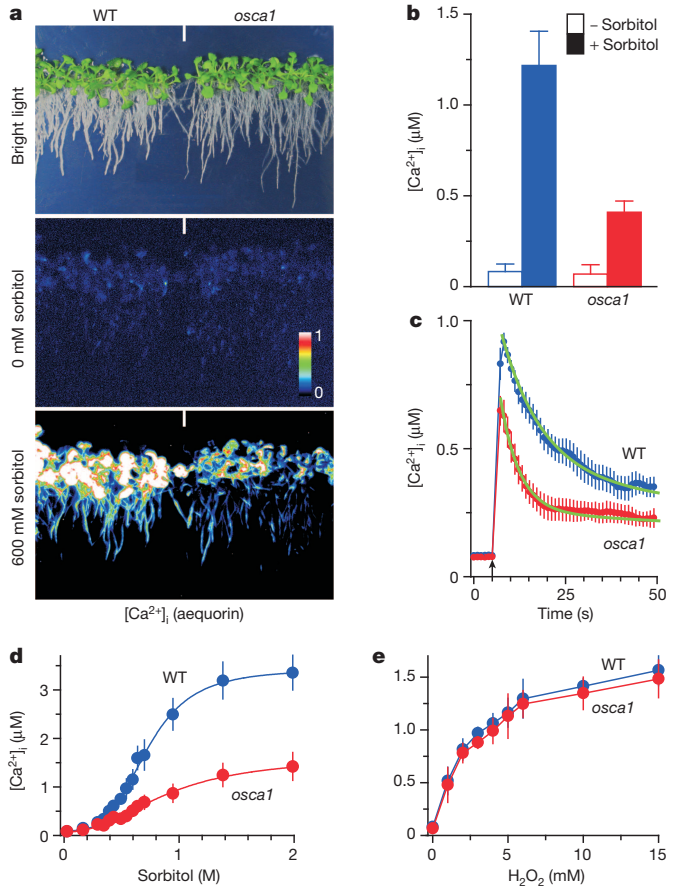

Figure 1 | Isolation of a genetic mutant with reduced hyperosmolality-induced $[Ca^{2+}]_i$ increases (OICI) in *Arabidopsis*. **a**, OICIs in wild-type (WT) and *osca1* plants. Plants expressing aequorin were treated with 0 or 600 mM sorbitol, and $[Ca^{2+}]_i$ was analysed by imaging aequorin. $[Ca^{2+}]_i$ is scaled by a pseudo-colour bar. **b**, Quantification of OICI in leaves from experiments similar to those in **a**. Data for three representative experiments are shown (mean ± standard error of the mean (s.e.m.); $n = 30$). **c**, Time-course analysis of OICI. Plants grown individually in a 96-well plate were treated with 600 mM sorbitol, and luminescence was recorded at intervals of 1 s. Data for 16 seedlings are shown (mean ± s.e.m.; two-way analysis of variance (ANOVA), $P < 0.001$). **d**, Increases in $[Ca^{2+}]_i$ plotted as a function of applied sorbitol concentrations. Data for three separate experiments are shown (mean ± standard deviation (s.d.); $n = 30$) and fitted to the Hill equation. **e**, Increases in $[Ca^{2+}]_i$ plotted as a function of applied H_2O_2 concentrations (mean ± s.d.; $n = 30$; two-way ANOVA, $P > 0.3$).

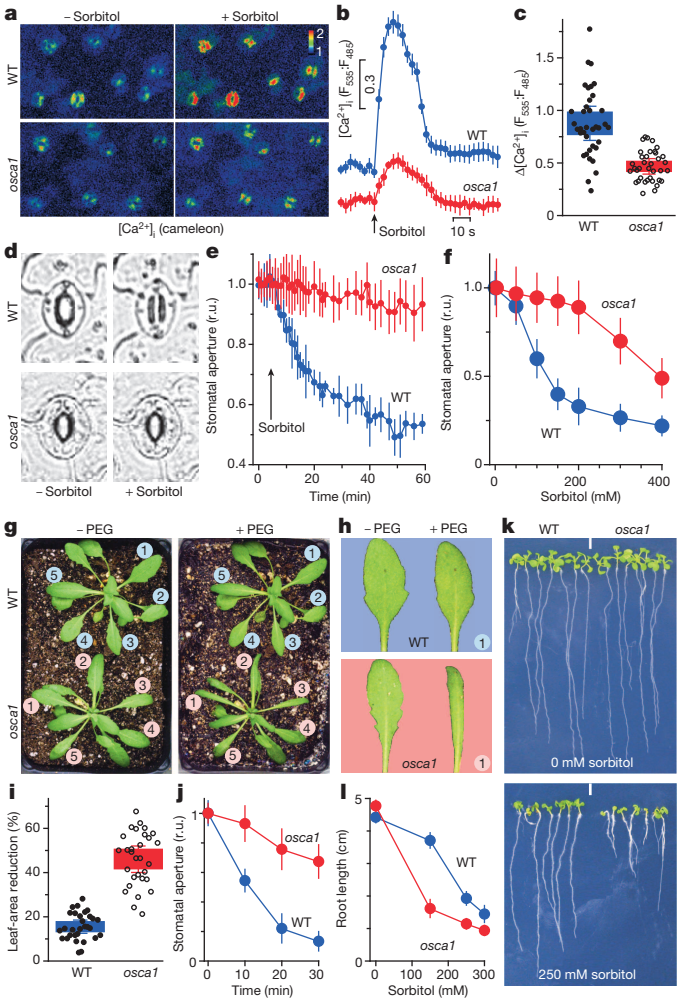

Figure 2 | Impaired guard cell osmotic stress signalling and attenuated plant responses to osmotic stress in osca1 plants. **a**, Emission images (F535 nm and F485 nm) of epidermal strips from plants expressing YC3.6 were taken every 3 s, and ratiometric images (F535:F485) before and 20 s after addition of 200 mM sorbitol are shown. **b**, The ratios were quantified from guard cell pairs in **a** ($n = 5$). **c**, Peak ratio changes from experiments similar to **a** and **b** are shown (boxes represent the standard error (s.e.), error bars are s.d.; $n = 36$; $P < 0.001$). **d**, Light images of epidermal strips were taken at varied intervals, and guard cell images before and 30 min after addition of 200 mM sorbitol are shown. **e**, Changes in the width of stomatal pores in response to sorbitol from the same epidermal strips in **d** (mean ± s.e.m.; $n = 5$ stomata; two-way ANOVA, $P < 0.001$; r.u., relative units). **f**, Stomatal apertures are plotted as a function of applied sorbitol concentrations (mean ± s.e.m.; $n = 80$ for 150 mM and 200 mM, and 60 for others; two-way ANOVA, $P < 0.001$). The apertures of wild type and *osca1* before the sorbitol treatment were 3.19 μm and 3.05 μm, respectively, and arbitrarily set to 1. **g**, Wild-type and *osca1* plants grown side-by-side in the same pot were treated with 20% PEG. Plant photos taken at time 0 and 30 min are shown. **h**, Leaves are numbered, and representative leaf no. 1 from **g** are shown. **i**, Leaf area reduction was quantified from experiments similar to those in **g**. Data from six independent experiments are shown (boxes represent the s.e., error bars are s.d.; $n = 30$; $P < 0.001$). **j**, PEG-induced stomatal closure from experiments similar to those in **g** was quantified. Stomatal apertures (width) at time 0 were 2.61 μm and 2.99 μm for wild type and *osca1*, respectively, and arbitrarily set to 1. Data from three independent experiments are shown (mean ± s.d.; $n = 60$; two-way ANOVA, $P < 0.01$). **k**, **l**, Plants were grown in half strength Murashige and Skoog medium (½ MS) in the presence or absence of sorbitol for 10 days (**k**) and root length was quantified (**l**). Data are from ten independent experiments (mean ± s.e.m.; $n = 60$; two-way ANOVA, $P < 0.001$).

the gateways for water loss and CO_2 uptake, and open and close in response to water availability[4]. The addition of 200 mM sorbitol caused stomatal closure in wild-type plants but this was much reduced in *osca1* plants (Fig. 2d, e). Through analysing the steady-state responses of stomatal apertures to sorbitol, we confirmed that the *osca1* mutant was less sensitive than wild-type plants (Fig. 2f). The dose-dependence data were fitted to the Hill equation with a K_d of 102 ± 2 mM and 323 ± 39 mM for wild-type and *osca1* plants, respectively. Note that the high apparent K_d values for OICIs observed in leaves might result from the slow penetration of solution through stomatal pores (Supplementary Information). Osmotic stress induces the accumulation of ABA, which triggers stomatal closure[3,4]. Nevertheless, ABA-induced stomatal closure was unaffected in *osca1* (Extended Data Fig. 3a), suggesting that OSCA1 may act upstream of ABA. These data indicate that OSCA1 may have a role in the calcium-mediated osmotic signalling in guard cells.

To understand whether OSCA1 has a key role in response to osmotic stress at the whole-plant level, we directly monitored plant wilting under osmotic stress. We treated wild-type and *osca1* plants with 20% polyethylene glycol (PEG). The leaf areas were reduced much more in *osca1* than those in wild-type plants (Fig. 2g–i), consistent with the observations that stomata were more open in *osca1* over the period of PEG

treatment (Fig. 2j) and that detached *osca1* leaves lost water more rapidly than wild type (Extended Data Fig. 3b).

We then examined long-term developmental responses to osmotic stress. Without osmotic stress wild-type and *osca1* seedlings had similar root lengths, while sorbitol treatment inhibited root growth more in *osca1* (Fig. 2k, l). Nevertheless, root growth in response to ABA was not affected in *osca1* (Extended Data Fig. 3c). These analyses reveal that *osca1* displays defects in major aspects of the osmotic stress signalling pathway as well as whole-plant responses to osmotic stress, indicating a defect in the perception of hyperosmolality.

Note that the *osca1* plants could not be distinguished from wild type throughout developmental stages, and that the phenotypes other than the reduced OICI were either impractical to map or were not robust enough to allow mapping of the *osca1* mutation, explaining why *osca1* mutants have not been isolated by previous forward genetic screens. Genetic analysis showed that the *osca1* phenotype was caused by a recessive mutation in a single nuclear gene (Extended Data Fig. 4a). We attempted to prepare a mapping population by crossing *osca1* (Col-0) as well as other mutants with reduced OICI to the most commonly used ecotype, Landsberg erecta. Unfortunately, it was not feasible to phenotype the F_2 and F_3 populations, possibly because variations introduced by the crosses between the two diverged ecotypes impaired the recognition of mutants having a relatively subtle phenotype. We tested several other commonly used ecotypes, and found that Wassilewskija (Ws) was the best (Extended Data Fig. 4a, b). We used ~12,600 F_2 seeds from the *osca1* × Ws cross, phenotyped their F_3 seedlings, and obtained 628 mapping lines. Note that the disadvantage of using Ws was the lack of a whole-genome sequence at the time, and we had to develop DNA markers based on available single nucleotide polymorphisms (SNPs) (Extended Data Fig. 4c).

Through fine mapping, *OSCA1* was identified as a novel gene encoding a protein of 772 amino acid residues (At4g04340; Extended Data Fig. 4d). Two nucleotide mutations were found in *osca1*, which resulted in mutations of glycine 59 to arginine (G59R) and glycine 507 to aspartic acid (G507D). Hydrophobicity analyses predicted OSCA1 as an integral protein with nine transmembrane α-helices (Fig. 3a and Extended Data Fig. 5). The region between transmembrane helices 8 and 9 could be another transmembrane helix, or a re-entrant pore loop. To verify whether

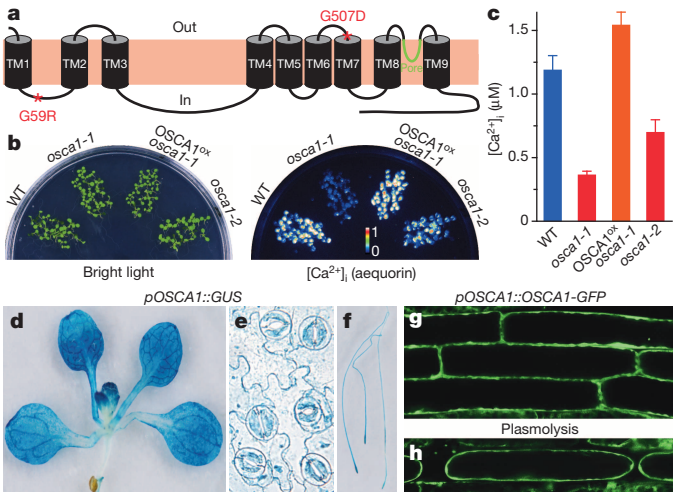

Figure 3 | *OSCA1* encodes a novel integral protein in the plasma membrane. **a**, The predicted membrane topology and protein structure of OSCA1. Transmembrane domains (TM), the pore domain and the two mutations in *osca1* are indicated. **b**, Complementation of the *osca1* phenotype by overexpression of OSCA1 ($OSCA^{ox}$ *osca1-1*). *osca1-2*, a T-DNA insertion line. **c**, Quantitative analysis of OICI in leaves from experiments as in **b** (mean ± s.e.m.; $n = 30$ seedlings). **d**–**f**, Expression patterns of *OSCA1* promoter *(pOSCA1)::GUS* in leaves (**d**), guard cells (**e**) and roots (**f**). **g**, **h**, Plasma membrane localization of OSCA1 in seedlings expressing the OSCA1 promoter-driven OSCA1–GFP construct. GFP fluorescence was observed in the periphery of the turgid cells (**g**) and plasmolysed cells (**h**).

OSCA1 is responsible for these phenotypes, we found that a T-DNA-insertion-mutagenized line, *osca1-2*, had a reduced OICI phenotype similar to *osca1* (Fig. 3b, c and Extended Data Fig. 6a–c). Note that *osca1* is *osca1-1* in this study. Additionally, overexpression of OSCA1 could complement the *osca1* phenotype.

To understand the molecular mechanisms and physiological functions of OSCA1 in plants, we determined the expression patterns and subcellular localization of OSCA1. Analysis of *OSCA1* promoter::*β-glucuronidase* (*GUS*) transgenic plants shows that OSCA1 was expressed in leaves, flowers and roots, and guard cells (Fig. 3d–f and Extended Data Fig. 6d–g). Similar patterns were seen in whole-plant GFP images of *OSCA1* promoter::*OSCA1-GFP* transgenic plants (Extended Data Fig. 6h, i), consistent with the reduced OICI phenotypes seen in leaves and roots, as well as in guard cells. OSCA1–GFP was exclusively localized to the vicinity of the cell surface in turgid cells (Fig. 3g and Extended Data Fig. 6j) as well as plasmolysed cells (Fig. 3h); while GFP alone was localized throughout the cells (Extended Data Fig. 6k). The plasma membrane localization is consistent with the prediction by the subcellular location database for *Arabidopsis* proteins[18], and supported by studies on plasma membrane proteomes[19,20].

To determine if OSCA1 can directly mediate Ca^{2+} influx, we expressed OSCA1 in human embryonic kidney 293 (HEK293) cells, and analysed its activity using Fura-2-based Ca^{2+} imaging. We postulated that increasing the Ca^{2+} concentration outside the cell might cause $[Ca^{2+}]_i$ elevation in cells overexpressing calcium-permeable channels even in the absence of the appropriate gating components. The elevation of external Ca^{2+} from 0.1 mM to 2.5 mM induced much larger $[Ca^{2+}]_i$ increases in cells expressing OSCA1 than those expressing an empty vector pcDNA3.2, or mutant OSCA1 (mOSCA1), which contains the two mutations identified in *osca1* plants (OSCA1(G59R/G507D) (mOSCA1)); Extended Data Fig. 7a–e). We then determined if OSCA1 could mediate OICIs. Addition of sorbitol triggered larger $[Ca^{2+}]_i$ increases in cells expressing OSCA1 than cells harbouring an empty vector (Extended Data Fig. 7f, g) or mOSCA1 (Fig. 4a–d). We determined the subcellular localization of OSCA1 and observed that only OSCA1–GFP was localized in the vicinity of the plasma membrane (Fig. 4e and Extended Data Fig. 8a, b). We employed the widely used Mn^{2+} quenching of Fura-2 fluorescence to monitor Ca^{2+} entry into the cell. The addition of Mn^{2+} resulted in a pronounced quenching of Fura-2 fluorescence in OSCA1-expressing cells, but to a much lesser extent in cells expressing an empty vector or mOSCA1 (Extended Data Fig. 8c). Together, these data demonstrate that expression of OSCA1 promotes Ca^{2+} influx across the plasma membrane in response to Ca^{2+} and hyperosmolality.

To determine if OSCA1 functions as a calcium-permeable channel gated by hyperosmolality, we carried out a series of electrophysiological experiments at the whole-cell and single-channel levels in HEK293 cells. The OSCA1-transfected cells showed larger currents in response to sorbitol treatment than GFP- or mOSCA1-transfected cells (Fig. 4f–i). The currents were enhanced at both positive and negative membrane potentials in a dose-dependent manner (Fig. 4g, j). A Hill curve could be fitted to the data with a K_d of 312 ± 12 mM and a Hill coefficient of 4.3. The similar Hill coefficients of ~4 obtained in plants and *in vitro* may be associated with tetrameter structures commonly seen for ion channels[10,11,21].

Given that the hyperosmolality-gated OSCA1-mediated currents decayed very fast, and that OSCA1-mediated currents were larger than the control under iso-osmotic conditions, as well as calcium-induced $[Ca^{2+}]_i$ increases in OSCA1-expressing cells, we characterized the electrophysiological properties of OSCA1 under iso-osmotic conditions with the expectation that the residual currents could represent largely those activated by hyperosmolality. The OSCA1-mediated currents appeared instantaneous, and showed a weak outward rectification (Fig. 4k and Extended Data Fig. 8d). We recorded OSCA1-mediated single-channel currents using outside-out membrane patches (Fig. 4l), these currents were not found in control cells or mOSCA1-expressing cells ($n > 25$ patches). The current–voltage relation gave rise to a conductance of 49.2 ± 5.5 pS (Extended Data Fig. 8e; $n = 5$). To determine the ionic

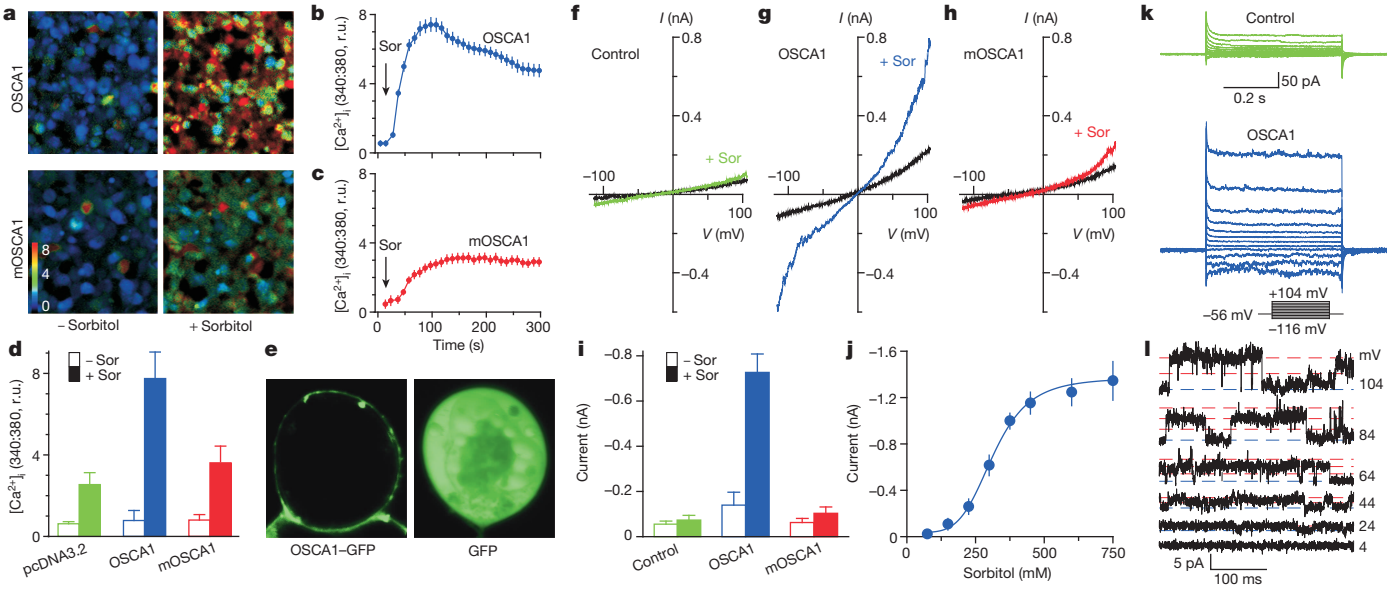

Figure 4 | OSCA1 forms hyperosmolality-gated calcium-permeable channels in HEK293 cells. **a**, Increases in $[Ca^{2+}]_i$ in response to 650 mM sorbitol in HEK293 cells expressing OSCA1, or mutant OSCA1 (OSCA1(G59R/G507D) (mOSCA1)). $[Ca^{2+}]_i$ increases were analysed by Fura-2 emission ratios (F340 nm:F380 nm) and scaled using a pseudo-colour bar. **b**, **c**, Dynamic analyses of OICI in cells expressing OSCA1 (**b**) or mOSCA1 (**c**) from experiments as in **a**. Data are mean ± s.d. ($n = 60$); Sor indicates point of sorbitol administration. **d**, Quantitative analyses of the OICI peaks from experiments as in **b**, **c** and Extended Data Fig. 7g. Data for three separate experiments are shown (mean ± s.e.m.). + Sor and − Sor, with and without the sorbitol treatment, respectively. pcDNA3.2, empty vector. **e**, Plasma membrane localization of OSCA1 in cells expressing OSCA1–GFP construct with GFP construct as a control. **f**–**h**, Whole-cell currents recorded during rapid voltage ramps (+124 mV to –116 mV) in cells expressing empty vector (**f**), OSCA1 (**g**) or mOSCA1 (**h**). Currents were recorded in the standard bath solution (black), and then with 300 mM sorbitol (green). Currents were recorded every 10 s with the largest currents shown. **i**, Averaged currents at –56 mV from experiments similar to these in **f**–**h** (mean ± s.e.m.; $n = 23$ (Control), 22 (OSCA1), 8 (mOSCA1)). **j**, Currents plotted as a function of applied sorbitol concentrations (mean ± s.e.m.; $n = 3$ (75 mM, 150 mM, 225 mM), 5 (600 mM, 750 mM), 22 (300 mM, 375 mM, 450 mM)) and fitted to the Hill equation. **k**, Whole-cell currents in cells expressing OSCA1 or the GFP vector as a control. **l**, Single-channel currents recorded in the outside-out patch from OSCA1-expressing cells.

selectivity of OSCA1 channels, we substituted cationic compositions in the bath and recorded currents (Extended Data Fig. 8f). The OSCA1 channel did not discriminate between monovalent and divalent cations, and had a slight preference for K^+, showing the following permeability sequence: $K^+ > Ba^{2+} \approx Ca^{2+} > Na^+ = Mg^{2+} = Cs^+$ (Extended Data Fig. 8g). Our data show that OSCA1 is a hyperosmolality-gated non-selective cation channel that permeates Ca^{2+} ions.

It is well established that various abiotic and biotic stimuli trigger $[Ca^{2+}]_i$ increases by activating Ca^{2+} channels in plants[6,9,22–24]. OSCA1 represents, to our knowledge, the first example of such a channel that has been identified genetically. OSCA1 was involved in osmotic-stress-induced fast signalling events, intermediate cellular processes and prolonged growth and development responses, and was also activated by hyperosmolality, similar to the osmosensor TRPV4 (ref. 25), revealing OSCA1 to be an osmosensor. Life largely involves aqueous chemistry as most cells consist of over 80% water[2,7]. A change in osmolality generates a stretch force on the plasma membrane, which activates osmosensors. Thus, osmosensors are known to be a subtype of mechanosensing channels such as DEG/ENaC, TRP, K2P, MscS-like and Piezo in non-plant eukaryotes[7,8,21,26]. No DEG/ENaC or TRP exist in plants[10,11]. Although there are ten MscS-like and one Piezo homologues in *Arabidopsis*[9], whether they function as osmosensors remains to be determined. The *Arabidopsis* MID1-complementing activity 1 and 2 (MCA1 and MCA2) proteins, which display homology to a yeast stretch-activated Ca^{2+} channel MID1, mediate hypo-osmolality-induced $[Ca^{2+}]_i$ increases and mechanical responses, but they are not pore-forming subunits[27]. *Arabidopsis thaliana* histidine kinase HK1 may function similarly to the yeast osmosensor histidine kinase SLN1 (ref. 28). Therefore, it would be interesting to study whether and how OSCA1 works together with those sensors to monitor water availability in plants.

OSCA1 belongs to a gene family with 15 members in *Arabidopsis*, and homologues are found in other plant species and throughout eukaryotes (Extended Data Figs 9 and 10). The yeast homologue RSN1 is a plasma membrane protein with unknown function (Supplementary Information)[29]. The founding member (OSCA3.1) of the family encoded early responsive to dehydration 4 protein (ERD4)[30]. Nonetheless, we found that ERD4 knockout mutants displayed wild-type OICIs, suggesting that ERD4 may differ from OSCA1, reminiscent of the diverse functions of TRPs in animals[26]. Identification of OSCA1 not only opens up a new avenue for studying osmosensing, but also sheds light on the molecular nature of Ca^{2+} channels responsible for other stimuli, and may provide potential molecular genetic targets for engineering crops resistant to drought.

Online Content Methods, along with any additional Extended Data display items and Source Data, are available in the online version of the paper; references unique to these sections appear only in the online paper.

Received 11 March; accepted 18 June 2014.
Published online 27 August 2014.

1. Zhu, J. K. Salt and drought stress signal transduction in plants. *Annu. Rev. Plant Biol.* **53,** 247–273 (2002).
2. Hsiao, T. C. Plant responses to water stress. *Annu. Rev. Plant Physiol. Plant Mol. Biol.* **24,** 519–570 (1973).
3. Cutler, S. R., Rodriguez, P. L., Finkelstein, R. R. & Abrams, S. R. Abscisic acid: emergence of a core signaling network. *Annu. Rev. Plant Biol.* **61,** 651–679 (2010).
4. Kim, T. H., Bohmer, M., Hu, H. H., Nishimura, N. & Schroeder, J. I. Guard cell signal transduction network: advances in understanding abscisic acid, CO_2, and Ca^{2+} signaling. *Annu. Rev. Plant Biol.* **61,** 561–591 (2010).
5. Knight, H., Trewavas, A. J. & Knight, M. R. Calcium signalling in *Arabidopsis thaliana* responding to drought and salinity. *Plant J.* **12,** 1067–1078 (1997).
6. Dodd, A. N., Kudla, J. & Sanders, D. The language of calcium signaling. *Annu. Rev. Plant Biol.* **61,** 593–620 (2010).
7. Kung, C. A possible unifying principle for mechanosensation. *Nature* **436,** 647–654 (2005).
8. Arnadóttir, J. & Chalfie, M. Eukaryotic mechanosensitive channels. *Annu. Rev. Biophys.* **39,** 111–137 (2010).
9. Monshausen, G. B. & Gilroy, S. Feeling green: mechanosensing in plants. *Trends Cell Biol.* **19,** 228–235 (2009).

10. Hedrich, R. Ion channels in plants. *Physiol. Rev.* **92,** 1777–1811 (2012).
11. Ward, J. M., Maser, P. & Schroeder, J. I. Plant ion channels: gene families, physiology, and functional genomics analyses. *Annu. Rev. Physiol.* **71,** 59–82 (2009).
12. Choi, J. *et al.* Identification of a plant receptor for extracellular ATP. *Science* **343,** 290–294 (2014).
13. Ranf, S. *et al.* Defense-related calcium signaling mutants uncovered via a quantitative high-throughput screen in *Arabidopsis thaliana*. *Mol. Plant* **5,** 115–130 (2012).
14. Pei, Z.-M. *et al.* Calcium channels activated by hydrogen peroxide mediate abscisic acid signalling in guard cells. *Nature* **406,** 731–734 (2000).
15. Monshausen, G. B., Messerli, M. A. & Gilroy, S. Imaging of the Yellow Cameleon 3.6 indicator reveals that elevations in cytosolic Ca^{2+} follow oscillating increases in growth in root hairs of *Arabidopsis*. *Plant Physiol.* **147,** 1690–1698 (2008).
16. Allen, G. J. *et al.* A defined range of guard cell calcium oscillation parameters encodes stomatal movements. *Nature* **411,** 1053–1057 (2001).
17. Roelfsema, M. R. G. & Hedrich, R. Making sense out of Ca^{2+} signals: their role in regulating stomatal movements. *Plant Cell Environ.* **33,** 305–321 (2010).
18. Tanz, S. K. *et al.* SUBA3: a database for integrating experimentation and prediction to define the SUBcellular location of proteins in *Arabidopsis*. *Nucleic Acids Res.* **41,** 1185–1191 (2013).
19. Zhang, Z. J. & Peck, S. C. Simplified enrichment of plasma membrane proteins for proteomic analyses in *Arabidopsis thaliana*. *Proteomics* **11,** 1780–1788 (2011).
20. Nühse, T. S., Stensballe, A., Jensen, O. N. & Peck, S. C. Large-scale analysis of *in vivo* phosphorylated membrane proteins by immobilized metal ion affinity chromatography and mass spectrometry. *Mol. Cell. Proteomics* **2,** 1234–1243 (2003).
21. Coste, B. *et al.* Piezo proteins are pore-forming subunits of mechanically activated channels. *Nature* **483,** 176–181 (2012).
22. Ding, J. P. & Pickard, B. G. Mechanosensitive calcium-selective cation channels by temperature. *Plant J.* **3,** 713–720 (1993).
23. Demidchik, V., Davenport, R. J. & Tester, M. Nonselective cation channels in plants. *Annu. Rev. Plant Biol.* **53,** 67–107 (2002).
24. Cosgrove, D. J. & Hedrich, R. Stretch-activated chloride, potassium, and calcium channels coexisting in plasma membranes of guard cells of *Vicia faba* L. *Planta* **186,** 143–153 (1991).
25. Liedtke, W. *et al.* Vanilloid receptor-related osmotically activated channel (VR-OAC), a candidate vertebrate osmoreceptor. *Cell* **103,** 525–535 (2000).
26. Wu, L. J., Sweet, T. B. & Clapham, D. E. International union of basic and clinical pharmacology. LXXVI. Current progress in the mammalian TRP ion channel family. *Pharmacol. Rev.* **62,** 381–404 (2010).
27. Nakano, M., Iida, K., Nyunoya, H. & Iida, H. Determination of structural regions important for Ca^{2+} uptake activity in *Arabidopsis* MCA1 and MCA2 expressed in yeast. *Plant Cell Physiol.* **52,** 1915–1930 (2011).
28. Wohlbach, D. J., Quirino, B. F. & Sussman, M. R. Analysis of the *Arabidopsis* histidine kinase ATHK1 reveals a connection between vegetative osmotic stress sensing and seed maturation. *Plant Cell* **20,** 1101–1117 (2008).
29. Wadskog, I. *et al.* The yeast tumor suppressor homologue Sro7p is required for targeting of the sodium pumping ATPase to the cell surface. *Mol. Biol. Cell* **17,** 4988–5003 (2006).
30. Kiyosue, T., Yamaguchishinozaki, K. & Shinozaki, K. Cloning of cDNAs for genes that are early-responsive to dehydration stress (ERDs) in *Arabidopsis thaliana* L.: identification of 3 ERDs as HSP cognate genes. *Plant Mol. Biol.* **25,** 791–798 (1994).

Supplementary Information is available in the online version of the paper.

Acknowledgements We thank M. R. Knight for providing an aequorin vector and aequorin expressing *Arabidopsis* seeds, S. Gilroy for a YC3.6 vector and YC3.6 expressing *Arabidopsis* seeds, M. R. Knight and S. Gilroy for sharing unpublished data on genetic screening and physical mapping, X. Dong and M. Chen for advice on physical mapping, J. Grandl, G. Chen and Q. Liu for advice concerning electrophysiology, W. G. Zhang and M. H. Zhu for providing HEK293 cells and advice on transfection, Y. Gao and S. Johnson for confocal imaging, and D. R. McClay, T.-p. Sun, J. Grandl and P. N. Benfey for discussions and critical reading of the manuscript. F.Y. and J.Z. were supported in part by grants from Hangzhou Normal University (PanDeng11001008001) and Zhejiang NSF (Z3110433). This work was supported by grants from USDA (CSREES-2005-35304-16196, CSREES-2006-35100-17304) and NSF (MCB-0451072, IOS-0848263) to Z.-M.P.

Author Contributions F.Y., H.Y., Y.X., D.K., R.Y., C.L., J.Z., T.S., B.K., D.M.J. and G.B.S. conducted aequorin imaging and genetic screen. F.Y., H.Y., Y.X., J.Z., L.T., conducted map-based cloning. F.Y., Y.X., D.K., R.Y. and Z.-M.P. conducted Ca^{2+} imaging and electrophysiological analyses in HEK293 cells and plant cells. F.Y., H.Y., Y.X., J.Z., L.T., T.S., B.K. and Y.H. carried out physiological analyses. Z.-M.P. designed the overall research with input from J.N.S. Z.-M.P., F.Y. and J.N.S. wrote the manuscript. All authors discussed the results and commented on the manuscript.

Author Information Reprints and permissions information is available at www.nature.com/reprints. The authors declare no competing financial interests. Readers are welcome to comment on the online version of the paper. Correspondence and requests for materials should be addressed to Z.-M.P. (zpei@duke.edu) or F.Y. (fangyuan@hznu.edu.cn).

METHODS

Plant material and growth conditions. *Arabidopsis thaliana* ecotype Col-0 constitutively expressing intracellular Ca^{2+} indicator aequorin (pMAQ2; a gift from M. Knight)[31] or constitutively expressing cameleon (YC3.6; a gift from S. Gilroy)[15] were used. The T-DNA insertion line SAIL_607_F09 (*osca1-2*), WiscDsLox331H10 (*osca1-3*), SALK_004685 (*erd4*) and SALK_078537.53.75.X (*erd4*)[30,32] were obtained from the *Arabidopsis* Biological Resource Center (ABRC). Plants were grown in soil (Scotts Metro-Mix 200), or in Petri dishes in half-strength Murashige and Skoog salts (1/2 MS; Sigma), 1.5% (w/v) sucrose (Sigma), and 0.8% (w/v) agar (Becton Dickinson) in controlled environmental rooms at 21 ± 2 °C. The fluency rate of white light was ~110 μmol m^{-2} s^{-1}. The photoperiods were 16 h light/8 h dark cycles. Seeds were sown on soil/MS media, placed at 4 °C for 4 days in the dark, and then transferred to growth rooms.

Aequorin bioluminescence-based Ca^{2+} imaging. $[Ca^{2+}]_i$ was measured using *Arabidopsis* plants expressing aequorin as described previously[31,33]. Seedlings were applied evenly with 3.3 ml of 10 μM coelenterazine (Prolume) per 150 mm × 15 mm Petri dish 12 h before imaging and placed in the dark. Aequorin bioluminescence imaging was performed using a ChemiPro HT system (Roper Scientific) equipped with a light-tight box, a cryogenically cooled and back-illuminated CCD camera and a liquid nitrogen autofiller. The camera was controlled by WinView/32 (Roper) and bioluminescence images were analysed using MetaMorph 6.3 (Molecular Devices). The recording of luminescence (L) was started 30 s prior treatments and lasted for 5 min. Bright-field images were taken after aequorin imaging. The total aequorin luminescence (L_{max}) was estimated by discharging with 0.9 M $CaCl_2$ in 10% (v/v) ethanol[31,33]. The calibration of $[Ca^{2+}]_i$ measurements was adopted from the equation described previously[34]: $pCa = 0.332588 \times (-\log k) + 5.5593$, where k is a rate constant equal to luminescence counts (L) divided by total remaining counts (L_{max}) with modification. Considering the previous equation was designed for aequorin luminometry spectroscopy, we used the measurement from a microplate luminescence reader (see below for details) to calibrate the ChemiPro HT system. We treated plants with 0 to 1 M sorbitol and obtained L/L_{max} values of leaves or roots. Then, we fit these data to the previous equation $pCa = a \times (-\log(L/L_{max})) + b$, and obtained the equation $pCa = 0.6747 \times (-\log k) + 5.3177$. Note that the calculated $[Ca^{2+}]_i$ presented in the current study are similar to those reported previously[5,34]. Data for dose-response curves were fitted to the Hill equation: $[Ca^{2+}]_i = [Ca^{2+}]_{i,max}$ $[sorbitol]^n/(K_d + [sorbitol]^n)$, where $[Ca^{2+}]_{i,max}$ is the maximum possible $[Ca^{2+}]_i$ change; [sorbitol], applied sorbitol concentration; K_d, the apparent dissociation constant; n, the Hill coefficient. All the treatments were carried out in the dark, and the experiments were carried out at room temperature (22−24 °C).

Screen for mutants with low OICI. *Arabidopsis* seeds expressing aequorin were mutagenized with ethyl methane sulphonate (EMS) as described previously[35]. Briefly, seeds (15 ml) were imbibed overnight and then shaken in 10 mM EMS for 15 h. The M1 seeds were rinsed thoroughly with tap water, mixed in 0.1% agarose, and planted in 40 flats (25.4 cm × 50.8 cm) at approximately 800 M1 seeds per flat. The flats were placed at 4 °C for 4 days before transfer to a greenhouse, and mature M2 seeds were collected in pools (~400 seedlings per pool). For screens for mutants with low hyperosmolality-induced $[Ca^{2+}]_i$ increase (OICI), M2 seeds were sterilized, and individual seeds were planted evenly using a template in 150 mm × 15 mm Petri dishes, and grown for 9 days. Aequorin bioluminescence images were acquired for the hyperosmolality treatment, that is, adding 600 mM sorbitol solution into Petri dish via a custom-built device. The total M2 seedlings that showed weaker $[Ca^{2+}]_i$ increases in leaves were picked up. These seedlings were then transferred to soil, and collected individually for seeds. From the second- to the fourth-round screens, individual lines were checked for the reduced OICI phenotype, and lines with the stable phenotype of low OICI were isolated as mutants with low OICI. To ensure that the low OICI phenotype was not caused by potential defects in aequorin-based calcium measurements, such as mutations in aequorin and the uptake of coelenterazine into to leaves, we sequenced the aequorin transgene in these putative mutants. In addition, we speculated that the reduced OICI phenotype should have cellular and physiological phenotypes in these putative mutants. Therefore, we analyzed known osmotic stress-regulated cellular and physiological processes and ranked these putative mutants based on these phenotypes for further mapping with the expectation that we could have a high probability to identify key components in the osmotic stress signaling pathway in plants.

Aequorin luminometry spectroscopy. Aequorin luminometry was carried out as described previously[5,31,34]. Aequorin-expressing *Arabidopsis* seeds of wild-type and *osca1* mutants were placed individually in each well in 96-well plates containing 50 μl ½ MS medium, 1.5% (w/v) sucrose, and 0.8% (w/v) agar, and grown for 10 days. Kinetic luminescence measurements were performed with an automated microplate luminescence reader (Mithras LB 940, Berthold Technologies). Luminescence counts were integrated every 1 s, and after automatic injection of 0.2 ml of 600 mM sorbitol solution into each well that took about 3 s, bioluminescence was recorded for 60 s per well. Luminescence values were calibrated as $[Ca^{2+}]_i$ using the following equation (ref. 34): $pCa = 0.332588 \times (-\log k) + 5.5593$.

Cameleon-based $[Ca^{2+}]_i$ imaging in guard cells and root cells. The *osca1-1* mutant was crossed into wild-type plants constitutively expressing GFP fluorescence resonance energy transfer (FRET)-based Ca^{2+} sensor yellow Cameleon 3.6 (YC3.6)[15,17,36], and five homozygous lines were generated. Cameleon-based $[Ca^{2+}]_i$ measurements in guard cells and root cells were conducted as described previously[16,37]. Rosette leaf epidermal peels from 2-week-old plants were placed in a microwell chamber in the bath solution containing 100 μM $CaCl_2$, 5 mM KCl, 10 mM MES-Tris, pH 6.15 for 2.5 h under light (120 μmol m^{-2} s^{-1}). Ratiometric Ca^{2+} imaging was performed using a fluorescence microscope (Axiovert 200; Zeiss) equipped with two filter wheels (Lambda 10-2; Sutter Instruments), and a cooled CCD camera (CoolSNAP$f\chi$; Roper Scientific). Excitation was provided at 440 nm, and emission ratiometric (F535 nm: F485 nm) images were collected using MetaFluor software. Hyperosmolality solutions were prepared by adding sorbitol to the bath solution, and epidermal peels were treated with these solutions at indicated time. Similarly, 5-day-old roots were used for YC3.6 imaging.

Stomatal aperture and density bioassays. The time course of stomatal response to treatments was examined as previously described with slight modifications[16]. Rosette leaf epidermal peels were placed in a microwell chamber and incubated in the opening solution containing 100 μM $CaCl_2$, 5 mM KCl, 10 mM MES-Tris, pH 6.15 for 2.5 h under light (120 μmol m^{-2} s^{-1}) as described above for imaging $[Ca^{2+}]_i$ in guard cells. Light images of epidermal peels were taken using the Axiovert 200 microscope at ~2 min intervals, and the width of stomatal apertures was analysed using ImageJ software (http://rsbweb.nih.gov/ij/index.html). Hyperosmolality solutions were prepared and added to the bath as described above. For the steady-state stomatal response to treatments of hyperosmolality and abscisic acid (ABA), experiments were carried out as described previously[14,38,39]. Detached rosette leaves of *Arabidopsis* were floated in the opening solution for 2.5 h under light. The leaves were transferred to the opening solution containing additional sorbitol or ABA at indicated concentrations for 2 h under light. Light images of epidermal peels were taken using the Axiovert 200 microscope, and the width of stomatal pore was analysed using ImageJ. Images of epidermal strips taken for stomatal aperture bioassay were reanalysed using ImageJ for stomatal densities and no difference of stomatal density between wild type and *osca1* was observed.

Physiological analyses in osmotic stress responses. Polyethylene glycol (PEG)-based osmotic stress treatments were adopted from the experimental procedure described previously[40]. Wild-type and *osca1* plants were grown side-by-side in the same pots with a hole in the bottom for 23 days, and the pots were submerged into a solution containing 20% (w/v) PEG-6000 (average molecular mass 6000; Sigma). Note that the rosette leaves did not contact the PEG solution. The 20% PEG treatment causes a modest osmotic stress (−0.5 mPa)[40]. Plants were photographed at 1 min intervals, and photographs at time 0 and 30 min were shown and used for further image analysis. Leaf areas for individual leaves were quantified using ImageJ, and leaf-area reduction for each leaf was calculated. For stomatal aperture analysis (Fig. 3d), seedlings were removed from pots that were submerged into the PEG solution at the indicated time. Epidermal strips were prepared immediately, and the width of stomatal apertures was analysed as described above. For leaf water loss assays, fully expanded rosette leaves were detached from 3-week-old seedlings and placed in the same growth conditions as described previously[40,41]. Each sample that had five individual leaves was weighed at the indicated time, and water loss was calculated in respect to the initial weight.

Genetic analysis and physical mapping. We back-crossed mutants with low OICI to aequorin-expressing Col-0 three times. The homozygous mutant lines in the Col-0 background that showed a 1:3 mutant:wild-type ratio were crossed to the ecotype Wassilewskija (Ws) and followed by self-pollinating F_1 progeny to yield an F_2 population. For *osca1* mapping, seedlings from ~12,600 F_2 seeds grown on Petri dishes that showed kanamycin resistance (aequorin transgene) were transferred to soil. Note that the mapping lines should be homozygous at both the aequorin and *osca1* loci. We genotyped aequorin using PCR, and aequorin-homozygous lines were then harvested individually for F_3 seeds. These F_3 lines were analysed individually for the reduced OICI phenotype using aequorin imaging. Eventually, homozygous osca1 lines with homozygous aequorin were obtained as the mapping population. Linkage analysis of F_2 plants revealed that the *osca1* locus is located in chromosome 4. Since at the time that we were carrying out the physical mapping there was no whole-genome sequence of Ws, we downloaded the 250,000 single-nucleotide polymorphism (SNP) data from the NSF 2010 Program (http://1001genomes.org/data/MPI/MPIcollab2011/releases/2011_06_28/strains/Ws-2/TAIR8/), and used the SNP information to design fine-mapping markers. Note that about 1 in 10 SNPs could be verified on average by sequencing and used for marker design. These markers were used to perform PCR and isolate the interval that flanks the mutation[42]. Finally, we sequenced open reading frames (ORFs) from the narrowest interval and identified mutations in *osca1*.

DNA constructs and transgenic lines. Gateway cloning[43] was used to construct *p35S::OSCA1*, *p35S::OSCA1-GFP*, *pOSCA1::GUS*, *pOSCA1::OSCA1-GFP*, *pCMV::OSCA1* and *pCMV::OSCA1-GFP*. The *OSCA1* full-length complementary DNA and the 2 kb promoter region were amplified by PCR from cDNA and genomic DNA, respectively. The cDNA fragment and the promoter region were cloned into the pENTR vector (Invitrogen). Coding sequences were transferred from the entry clones to gateway-compatible destination vectors (Invitrogen). Transgenic *Arabidopsis* lines were generated by agrobacteria-mediated transformation[44], and homozygous transgenic T3 lines carrying a single insertion were used. The *osca1-2* (SAIL_607_F09) and *osca1-3* (WiscDsLox331H10) lines were obtained from the ABRC. Homozygous lines were selected and the *OSCA1* transcript was analysed by reverse transcription PCR (RT–PCR). The *osca1-2* and *osca1-3* mutants were crossed into the aequorin-expressing wild-type, and homozygous lines were generated. Note that, in the *osca1-3* background, aequorin expression was silenced and several *osca1-3* aequorin lines identified could not be used to analyse the reduced OICI phenotype.

***OSCA1* mRNA analysis.** The abundance of *OSCA1* mRNAs from wild-type and *osca1* seedlings was analysed by RT–PCR as described[42]. Total mRNAs were prepared and reverse transcribed using a cDNA synthesis kit, and UBQ was used as a loading control[45].

Histochemical GUS activity analysis. The histochemical staining for β-glucuronidase (GUS) activity using the OSCA1-promoter-driven GUS (*pOSCA1::GUS*) transgenic lines was performed as described[37]. Seedlings grown in ½ MS media or the soil were used for the histochemical staining[46]. Data represent six independent lines examined, which displayed similar staining patterns. Similar results were seen from OSCA1-promoter-driven (OSCA1–GFP) (*pOSCA1::OSCA1-GFP*) transgenic lines.

OSCA1–GFP subcellular localization analysis. For analysis of OSCA1–GFP in *Arabidopsis* seedlings, both OSCA1 promoter-driven *pOSCA1::OSCA1-GFP* and 35S-promoter-driven *p35S::OSCA1-GFP* transgenic plants were generated as described[33,44]. The *p35S::GFP* transgenic plants were used as a control. Seedlings grown in ½ MS media in Petri dishes for 7 days were subjected to confocal imaging with the Zeiss LSM 710 microscope or whole seeding imaging with a Zeiss SteREO Discovery V20 microscope. Plasmolysis was developed by adding 0.8 M sorbitol. Data represent more than 10 independent lines examined, which displayed similar GFP subcellular localization. For analysis of OSCA1–GFP) in HEK293 cells, cells were cultured on poly-lysine-coated glass coverslips and transfected transiently with *pCMV::OSCA1-GFP* as described above. About 18 to 24 h after transfection, coverslips were mounted on glass slides and subjected immediately to GFP fluorescence imaging with the Zeiss Axiovert 200 microscope, as well as confocal imaging with the Zeiss LSM 710 microscope. For confocal imaging a ×63 water immersion objective was used. The plasma membrane localization is well supported by several studies on plasma membrane proteomes[19,20,47].

Imaging of $[Ca^{2+}]_i$ in HEK293 cells. Human embryonic kidney 293T (HEK293T) were grown and maintained in DMEM medium supplemented with 10% fetal bovine serum, 1% penicillin and streptomycin in a CO_2 incubator at 37 °C. For transfection, cells were seeded onto poly-lysine-coated eight-well chambered coverglasses (Nunc) overnight, and transfected with plasmid DNA using Lipofectamine 2000 reagent (Invitrogen) as described previously[37,48,49]. Cells were loaded with the Ca^{2+} sensitive dye Fura-2AM (5 μM; Sigma). A Fura-2-based Ca^{2+} imaging assay was performed in the HEK293 cells 18 to 24 h after transfection using the Axiovert 200 fluorescence microscope. Emission ratiometric images (F340 nm:F380 nm) were collected using MetaFluor Fluorescence Ratio Imaging Software (Molecular Devices). Experiments were carried out at room temperature (22–24 °C). For further analysis, about 25 to 30 cells per image were selected manually based on the increases in $[Ca^{2+}]_i$ (from highest to lowest). For Ca^{2+} treatment, Fura 2-loaded HEK293 cells were incubated in a standard buffer containing 130 mM NaCl, 3 mM KCl, 0.6 mM $MgCl_2$, 10 mM glucose, 10 mM HEPES, pH 7.4 (adjusted with NaOH), and 0.1 mM Ca^{2+} for 30 min. The bath was perfused using a peristaltic pump (Dynamax RP-1, Rainin) with a 2.5 mM Ca^{2+} solution prepared from adding Ca^{2+} into the standard buffer, and Fura-2 ratiometric images were collected. For the hyperosmotic treatment, solutions with different osmolality were prepared by adding sorbitol to a Na^+-free buffer containing 130 mM NMDG-Cl, 3 mM KCl, 2 mM $CaCl_2$, 0.6 mM $MgCl_2$, 10 mM glucose, 10 mM HEPES, pH 7.4 (adjusted with HCl). Unless otherwise described, the Ca^{2+} concentration of all solutions was held constant at 2 mM. Osmolality was measured with a vapour pressure osmometer (Vapro 5520, Wescor). The bath was perfused with hypertonic solutions, and Fura-2 ratiometric images were collected and analysed.

Mn^{2+} quenching of Fura-2 fluorescence. HEK293 cells were transfected and loaded with Fura-2AM as described above. Emission (510 nm) images with three excitation wavelengths (340 nm, 358 nm and 380 nm) were recorded. Quenching of the 358 nm signal, which is the calcium-independent wavelength of Fura-2 and reflects Mn^{2+} influx across the plasma membrane[50–52], was monitored subsequently in the presence of 1 mM Mn^{2+}. Background fluorescence was determined by supplementing the standard buffer with 10 μM Triton X-100 and 10 mM Mn^{2+}. The pcDNA3.2 empty vector-transfected cells were used as a negative control.

HEK293 cell electrophysiology. HEK293 cells were co-transfected with eGFP and OSCA1, mOSCA1 or pcDNA3.2 at a ratio of 1:20, plated on poly-L-lysine coated glass coverslips, and then recorded for electrophysiological signals[48,49]. Patch-clamp recordings were performed on eGFP-positive cells 24−36 h after transfection. Gigaohm-seals were obtained with pipettes (Kimax 51) having a resistance of 3–5 MΩ in a standard pipette solution (see below). Liquid junction potentials were measured and also calculated using pClamp 8.3 software (Molecular Devices), and correction for this offset was made as described in the software. Voltage-clamp experiments[14,48,49] were performed with Axopatch 200B patch-clamp amplifier (Molecular Devices), and data were acquired using Digidata 1322A interface and the pClamp software. The currents were recorded at a holding potential of −56 mV at room temperature and no leak subtraction was performed. Permeability ratios for monovalent cations to Cs^+ (PX/PCs) were calculated as follows: $PX/PCs = \exp(\Delta V_{rev}F/RT)$, where V_{rev} is the reversal potential, F is the Faraday's constant, R is the universal gas constant, and T is the absolute temperature[48,49,51]. Divalent permeability was calculated as, $PY/PCs = [Cs^+]_i \exp(\Delta V_{rev}F/RT)(1 + \exp(\Delta V_{rev}F/RT))/4[Y^{2+}]_o$, where the bracketed terms are ionic activities. Assumed ion activity coefficients were 0.75 for monovalents and 0.25 for divalents[53].

Solutions for electrophysiology. The standard pipette solution for all experiments contained 140 mM CsCl, 5 mM EGTA, 10 mM HEPES, pH 7.4 (adjusted with CsOH) as described[48,49,54]. The standard bath solution contained 140 mM NaCl, 5 mM KCl, 2 mM $MgCl_2$, 2 mM $CaCl_2$, 10 mM HEPES, 10 mM glucose, pH 7.4 (adjusted with NaOH). For monovalent-cation substitution experiments, the bath solution was changed to 140 mM NaCl (or KCl or CsCl), 10 mM glucose and 10 mM HEPES (adjusted to pH 7.4 with NaOH, KOH or CsOH, respectively). For divalent-cation substitution experiments, the bath solution was changed to 112 mM $CaCl_2$ (or $MgCl_2$), 10 mM glucose, 10 mM HEPES, pH 7.4 (adjusted with $Ca(OH)_2$ or $Mg(OH)_2$, respectively). Reversal potential was determined using voltage ramps (+100 to −100 mV in 1.56 s) and current clamps at 0 pA.

PCR primers and vectors. Genotyping primers: OSCA1-LP, 5′-TAACCATTCA GTTGGGTTTCG; OSCA1-RP, 5′-ATTGGACAAACAACGAGTTGG. T-DNA-LB, 5′-TCTGAATTTCATAACCAATCTCG. RT–PCR primers: OSCA1_Fw, 5′-TG CTTGCTTGGGCAGTTCTTGTA; OSCA1_Rev, 5′-GGCAAGAAACTGAAGC CTCATGT. UBQ_Fw, 5′-TAAAAACTTTCTCTCAATTCTCTCT, UBQ_Rev, 5′-TTGTCGATGGTGTCGGAGCTT. Cloning primers: OSCA1-cDNA_Fw, 5′-CACCATGGCAACACTTAAAGACATT; OSCA1-cDNA_Rev, 5′-(CTA)GACT TCTTTACCGTTAATAAC; OSCA1-eGFP_Fw, 5′-AAACTCGAGATGGCAAC ACTTAAAGACATTG; OSCA1-eGFP_Rev, 5′-AAACCGCGGGACTTCTTTAC CGTTAATAACGG. Primers for OSCA1 promoter: OSCA1P_Fw, 5′-CACCAG TCCCGCGATATTCAGC; OSCA1P_Rev, 5′-GCTTTGTTACTTTTGCTACTC CA. Vectors: pCMV::OSCA1:pcDNA3.2, pCMV::OSCA1-GFP:pEGFP-N1, p35S::OSCA1: pMDC32, pOSCA1::GUS:pMDC163, p35S::OSCA1-GFP:pMDC83, and pOSCA1::OSCA1-GFP:pMDC107. For mutant OSCA1 (mOSCA1) construct, the same two mutations (G59R and G507D) as in the *osca1* mutant were introduced in wild-type OSCA1, and the vector for mOSCA1 was pCMV::OSCA1(G59R/G507D):pcDNA3.2.

Gene accession numbers in GenBank. AtOSCA1.1, KJ920356; AtOSCA1.2, KJ920357; AtOSCA1.3, KJ920358; AtOSCA1.4, KJ920359; AtOSCA1.5, KJ920360; AtOSCA1.6, KJ920361; AtOSCA1.7, KJ920362; AtOSCA1.8, KJ920363; AtOSCA2.1, KJ920364; AtOSCA2.2, KJ920365; AtOSCA2.3, KJ920366; AtOSCA2.4, KJ920367; AtOSCA2.5, KJ920368; AtOSCA3.1, KJ920369; AtOSCA4.1, KJ920370; OsOSCA1.1, KJ920371; OsOSCA1.2, KJ920372; OsOSCA1.3, KJ920373; OsOSCA1.4, KJ920374; OsOSCA2.1, KJ920375; OsOSCA2.2, KJ920376; OsOSCA2.3, KJ920377; OsOSCA2.4, KJ920378; OsOSCA2.5, KJ920379; OsOSCA3.1, KJ920380; OsOSCA4.1, KJ920381.

Statistical analysis. Independent experiments were performed at least three times. The statistical analysis was performed using EXCEL 10 software (Microsoft). Data were presented as mean ± s.d. or s.e.m. To analyse the difference between genotypes two-way analysis of variance (ANOVA) was carried out using SAS 9.3 software (SAS Institute). For Fig. 2c, i and Extended Data Fig. 2g, the boxes represent s.e., the error bars represent s.d., and means were within the boxes. P values < 0.05 were considered statistically significant.

31. Knight, M. R., Campbell, A. K., Smith, S. M. & Trewavas, A. J. Transgenic plant aequorin reports the effects of touch and cold-shock and elicitors on cytoplasmic calcium. *Nature* **352,** 524–526 (1991).
32. Yamaguchishinozaki, K., Koizumi, M., Urao, S. & Shinozaki, K. Molecular-cloning and characterization of 9 cDNAs for genes that are responsive to desiccation in *Arabidopsis thaliana*: sequence-analysis of one cDNA clone that encodes a putative transmembrane channel protein. *Plant Cell Physiol.* **33,** 217–224 (1992).
33. Tang, R. H. *et al.* Coupling diurnal cytosolic Ca^{2+} oscillations to the CAS-IP3 pathway in *Arabidopsis*. *Science* **315,** 1423–1426 (2007).

34. Knight, H., Trewavas, A. J. & Knight, M. R. Cold calcium signaling in *Arabidopsis* involves two cellular pools and a change in calcium signature after acclimation. *Plant Cell* **8,** 489–503 (1996).
35. Koornneeff, M., Dellaert, L. W. M. & Vanderveen, J. H. EMS- and radiation-induced mutation frequencies at individual loci in *Arabidopsis thaliana* (L.) Heynh. *Mutat. Res.* **93,** 109–123 (1982).
36. Swanson, S. J., Choi, W. G., Chanoca, A. & Gilroy, S. In vivo imaging of Ca^{2+}, pH, and reactive oxygen species using fluorescent probes in plants. *Annu. Rev. Plant Biol.* **62,** 273–297 (2011).
37. Han, S. C., Tang, R. H., Anderson, L. K., Woerner, T. E. & Pei, Z.-M. A cell surface receptor mediates extracellular Ca^{2+} sensing in guard cells. *Nature* **425,** 196–200 (2003).
38. Pei, Z.-M., Ghassemian, M., Kwak, C. M., McCourt, P. & Schroeder, J. I. Role of farnesyltransferase in ABA regulation of guard cell anion channels and plant water loss. *Science* **282,** 287–290 (1998).
39. Pei, Z.-M., Kuchitsu, K., Ward, J. M., Schwarz, M. & Schroeder, J. I. Differential abscisic acid regulation of guard cell slow anion channels in *Arabidopsis* wild-type and abi1 and abi2 mutants. *Plant Cell* **9,** 409–423 (1997).
40. Verslues, P. E., Agarwal, M., Katiyar-Agarwal, S., Zhu, J. H. & Zhu, J. K. Methods and concepts in quantifying resistance to drought, salt and freezing, abiotic stresses that affect plant water status. *Plant J.* **45,** 523–539 (2006).
41. Osakabe, Y. *et al.* Osmotic stress responses and plant growth controlled by potassium transporters in *Arabidopsis*. *Plant Cell* **25,** 609–624 (2013).
42. He, Y. *et al.* Nitric oxide represses the *Arabidopsis* floral transition. *Science* **305,** 1968–1971 (2004).
43. Karimi, M., Inze, D. & Depicker, A. GATEWAY^{TM} vectors for *Agrobacterium*-mediated plant transformation. *Trends Plant Sci.* **7,** 193–195 (2002).
44. Clough, S. J. & Bent, A. F. Floral dip: a simplified method for Agrobacterium-mediated transformation of *Arabidopsis thaliana*. *Plant J.* **16,** 735–743 (1998).
45. Wang, Z.-Y. & Tobin, E. M. Constitutive expression of the CIRCADIAN CLOCK ASSOCIATED 1 (CCA1) gene disrupts circadian rhythms and suppresses its own expression. *Cell* **93,** 1207–1217 (1998).
46. Jefferson, R. A., Kavanagh, T. A. & Bevan, M. W. GUS fusions: beta-glucuronidase as a sensitive and versatile gene fusion marker in higher plants. *EMBO J.* **6,** 3901–3907 (1987).
47. Benschop, J. J. *et al.* Quantitative phosphoproteomics of early elicitor signaling in *Arabidopsis*. *Mol. Cell. Proteomics* **6,** 1198–1214 (2007).
48. McKemy, D. D., Neuhausser, W. M. & Julius, D. Identification of a cold receptor reveals a general role for TRP channels in thermosensation. *Nature* **416,** 52–58 (2002).
49. Caterina, M. J. *et al.* The capsaicin receptor: a heat-activated ion channel in the pain pathway. *Nature* **389,** 816–824 (1997).
50. Hashii, M. *et al.* Bradykinin B-2 receptor-induced and inositol tetrakisphosphate-evoked Ca^{2+} entry is sensitive to a protein tyrosine phosphorylation inhibitor in ras-transformed NIH/3T3 fibroblasts. *Biochem. J.* **319,** 649–656 (1996).
51. Hofmann, T. *et al.* Direct activation of human TRPC6 and TRPC3 channels by diacylglycerol. *Nature* **397,** 259–263 (1999).
52. Berbey, C. & Allard, B. Electrically silent divalent cation entries in resting and active voltage-controlled muscle fibers. *Biophys. J.* **96,** 2648–2657 (2009).
53. Valera, S. *et al.* New class of ligand-gated ion-channel defined by P2X receptor for extracellular ATP. *Nature* **371,** 516–519 (1994).
54. Peier, A. M. *et al.* A TRP channel that senses cold stimuli and menthol. *Cell* **108,** 705–715 (2002).
55. Knight, H. & Knight, M. R. Abiotic stress signalling pathways: specificity and cross-talk. *Trends Plant Sci.* **6,** 262–267 (2001).
56. McAinsh, M. R. & Pittman, J. K. Shaping the calcium signature. *New Phytol.* **181,** 275–294 (2009).
57. Yamaguchi-Shinozaki, K. & Shinozaki, K. Transcriptional regulatory networks in cellular responses and tolerance to dehydration and cold stresses. *Annu. Rev. Plant Biol.* **57,** 781–803 (2006).
58. Page, D. R. & Grossniklaus, L. The art and design of genetic screens: *Arabidopsis thaliana*. *Nature Rev. Genet.* **3,** 124–136 (2002).
59. Moller, S., Croning, M. D. R. & Apweiler, R. Evaluation of methods for the prediction of membrane spanning regions. *Bioinformatics* **17,** 646–653 (2001).
60. Schwacke, R. *et al.* ARAMEMNON, a novel database for *Arabidopsis* integral membrane proteins. *Plant Physiol.* **131,** 16–26 (2003).
61. Nuhse, T. S., Stensballe, A., Jensen, O. N. & Peck, S. C. Phosphoproteomics of the *Arabidopsis* plasma membrane and a new phosphorylation site database. *Plant Cell* **16,** 2394–2405 (2004).
62. Sievers, F. *et al.* Fast, scalable generation of high-quality protein multiple sequence alignments using Clustal Omega. *Mol. Syst. Biol.* **7,** 6 (2011).

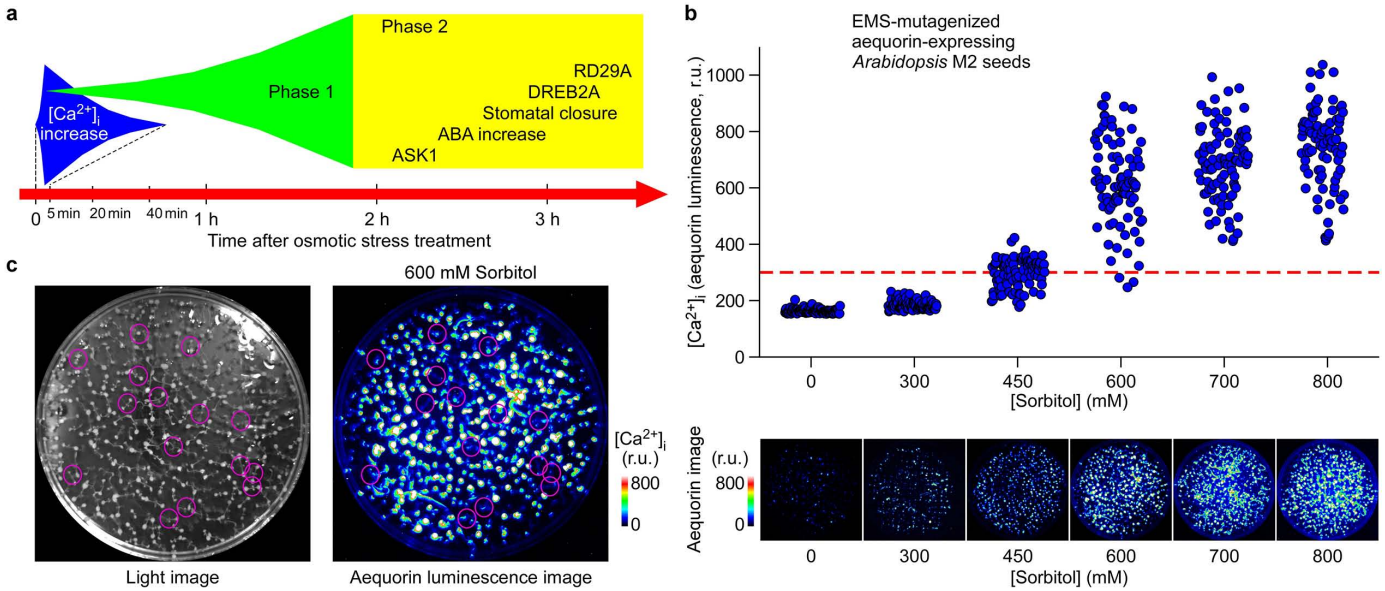

Extended Data Figure 1 | Events occurring after osmotic stress treatment, and optimized conditions for genetic screens for mutants with low hyperosmolality-induced $[Ca^{2+}]_i$ increases. **a**, Schematic illustration of events occurring after osmotic stress treatment. It is known that osmotic stress triggers a signalling cascade, in which the earliest detectable event is an increase in $[Ca^{2+}]_i$ that lasts ~5 min (blue)[5,55,56]. For immediate responses, the signal is funnelled to downstream events, such as the activation of ASK1 protein kinase, ABA accumulation and stomatal closure, leading to the reduction of water loss[4]. For sustainable responses, the expression profiles for many genes, such as *DREB2A* and *RD29A*, are altered[57]. Collectively, although these events might start as early as the $[Ca^{2+}]_i$ increase, they display a dynamic change (phase 1), and take a long time to reach a relative steady state (phase 2; Supplementary Information). Clearly, in contrast to traditional genetic screens, in which the phenotypes scored can take hours or days to reach a steady state[58], the entire transient OICI event lasts only ~5 min, which could be used to genetically dissect osmosensing. Recently, similar screens using pathogen elicitors and ATP have been carried out, while the associated Ca^{2+} channels have not been identified[12,13]. The amplitudes of coloured polygons depict the dynamic activities of these events evoked by osmotic stress. **b**, Optimized conditions for genetic screens for mutants with low hyperosmolality-induced $[Ca^{2+}]_i$ increases (OICI). EMS-mutagenized aequorin-expressing *Arabidopsis* M2 seeds were used to determine the optimum genetic screening conditions. Individual seeds were planted evenly using a template in 150 mm × 15 mm Petri dishes, and grown for 9 days. The sorbitol solution at an indicated concentration was added into the Petri dish, and the aequorin images were acquired. Sorbitol concentrations from 0 to 800 mM were tested and representative aequorin images are shown (bottom). Relative $[Ca^{2+}]_i$ in leaves is scaled by a pseudo-colour bar. Corresponding relative $[Ca^{2+}]_i$ for each individual seedling was analysed and plotted (top). At 600 mM sorbitol concentration, about 95% of seedlings showed an OICI using an artificial cut-off value (red line), which could be practically used to phenotype/score seedlings. Similar results were seen in more than 10 independent experiments and one representative experiment is shown. **c**, Isolation of individuals with low OICI in leaves in the first-round screen. The bright-field image was used to identify the position for each seedling (left). Individual seedlings with lower leaf OICI signals in the bioluminescence image (right) were circled via image analyses, and selected seedlings were transferred from the Petri dish to soil. At the first round we picked up seedlings with low leaf OICI signals as putative *osca1* candidates.

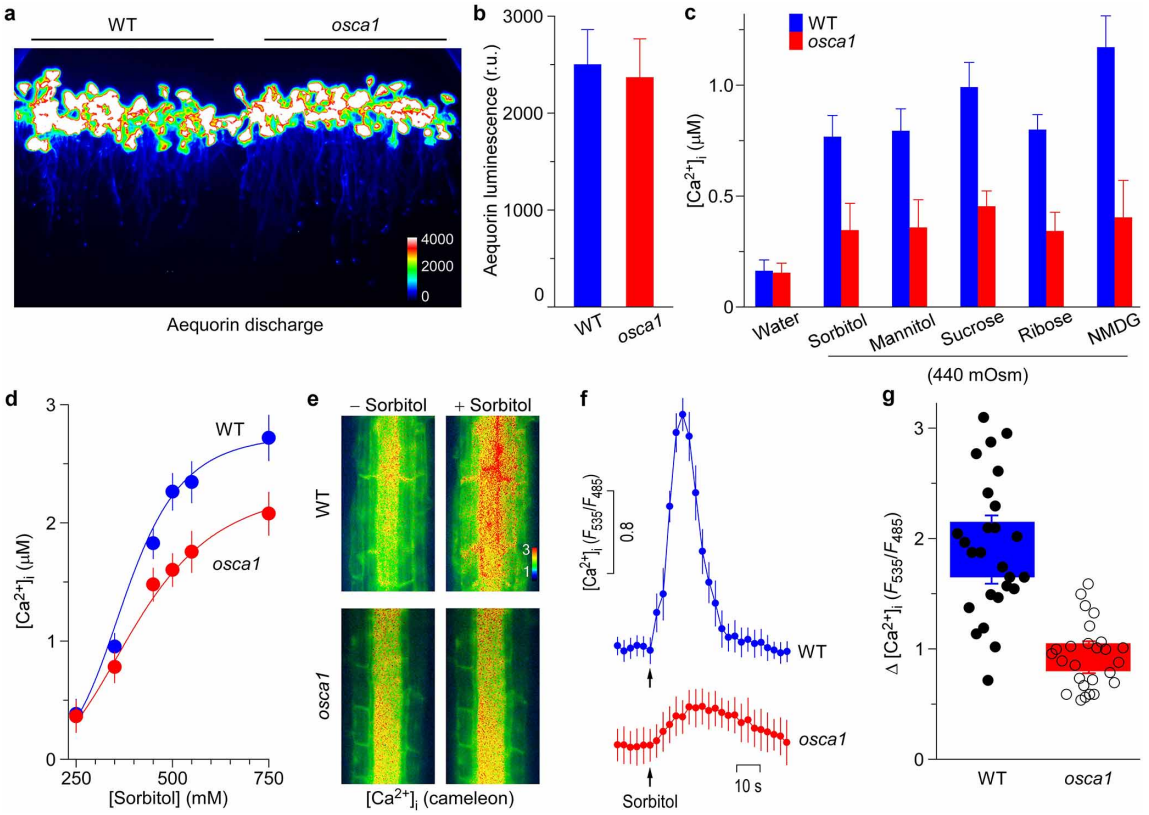

Extended Data Figure 2 | Defect in hyperosmolality-induced $[Ca^{2+}]_i$ increases in *osca1*. **a**, **b**, Similar total amount of aequorin in wild-type (WT) and *osca1* seedlings. The same seedlings used in Fig. 1a were treated with a solution containing 0.9 M $CaCl_2$ and 10% (v/v) ethanol to measure the total amount of aequorin, and no difference between wild type and *osca1* was observed (**a**). Similar results were seen in >20 separate experiments. Quantification of total amount of aequorin in wild-type and *osca1* plants from experiments as in **a** is plotted as mean ± s.e.m. (**b**; $n = 6$; $P > 0.8$). **c**, The *osca1* mutant shows reduced OICIs. The aequorin-expressing wild-type and *osca1* seedlings grown side-by-side were treated with water or 440 mOsm solutions containing sorbitol, mannitol, sucrose, ribose or *N*-methyl-D-glucamine (NMDG), and changes in $[Ca^{2+}]_i$ in leaves were recorded. Data are mean ± s.e.m. ($n = 33$ for sorbitol, 29 for mannitol and sucrose, 26 for ribose and 21 for NMDG). The responses to these compounds were significantly reduced in *osca1* compared to those in wild type ($P < 0.005$). **d**, Averaged increases in $[Ca^{2+}]_i$ in wild-type and *osca1* roots plotted as a function of applied sorbitol concentrations. Seedlings were grown in a Petri dish that was placed vertically similar to those in Fig. 1a, and aequorin images were acquired and analysed as in Fig. 1. Data for three separate experiments representing 30 seedlings are shown (mean ± s.d.; two-way ANOVA, $P < 0.01$). **e**–**g**, Reduced OICIs in root cells in *osca1*. FRET imaging of OICIs was carried out in root cells in wild-type and *osca1* plants expressing the Ca^{2+} indicator protein YC3.6. Emission images (F535 and F485) of roots were taken every 3 s, and ratiometric images before and 20 s after addition of 600 mM sorbitol are shown (**e**). The F535:F485 ratio is scaled by a pseudo-colour bar. The relative $[Ca^{2+}]_i$ (F535:F485) in response to sorbitol treatment was quantified from these root cells in **e** (**f**; mean ± s.e.m.; $n = 10$). Peak changes in ratios from experiments similar to **e** and **f** are shown (**g**; boxes represent s.e., error bars are s.d.; $n = 26$ seedlings; $P < 0.001$).

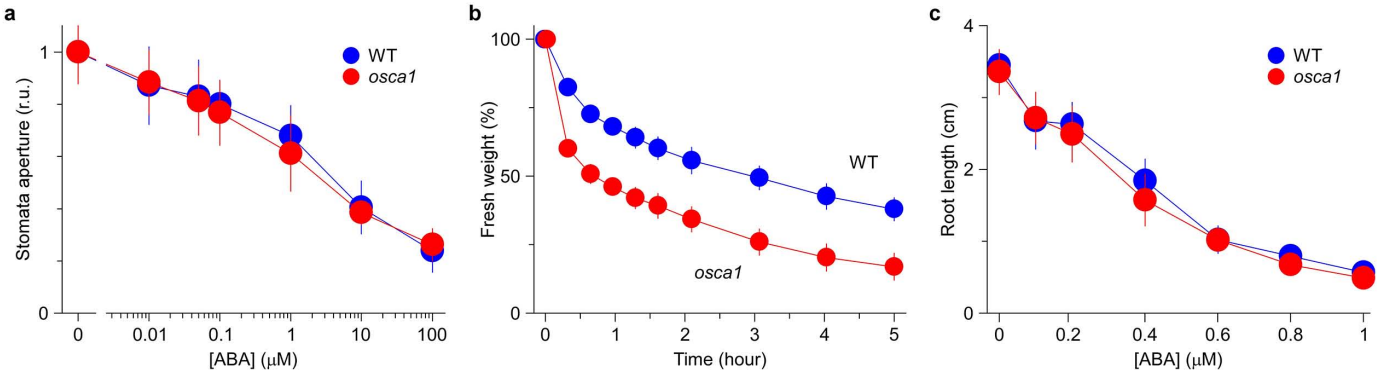

Extended Data Figure 3 | OSCA1 acts upstream of ABA signalling in stomatal closure and root growth. **a**, Comparison of ABA-induced stomatal closing in wild type and *osca1*. Data shown are mean ± s.e.m. ($n = 60$; two-way ANOVA, $P > 0.5$). Stomatal apertures were normalized with respect to the width in the absence of ABA. **b**, OSCA1 controls transpirational water loss in response to desiccation treatment. Rosette leaves from wild-type and *osca1* seedlings were detached, and transpirational water loss was analysed at the indicated time points after leaf detachment. Water loss was calculated as a percentage of the initial fresh weight. Data shown are mean ± s.e.m. ($n = 25$ leaves; two-way ANOVA, $P < 0.001$). **c**, Wild-type and *osca1* plants were grown in ½ MS media containing 0–1 μM ABA, and root lengths were analysed similarly as in Fig. 2k, l. Data from three independent experiments are shown (mean ± s.d.; $n = 30$ seedlings; two-way ANOVA, $P > 0.2$).

a

Crosses	Number of F2 plants		Ratio (WT : *osca1*)
	WT	*osca1*	
osca1 x Col_{AQ}	101.5 ± 4.5	35.5 ± 2.6	2.92 ± 0.27
osca1 x Ws	78.3 ± 1.7	27.8 ± 2.2	2.93 ± 0.24

b

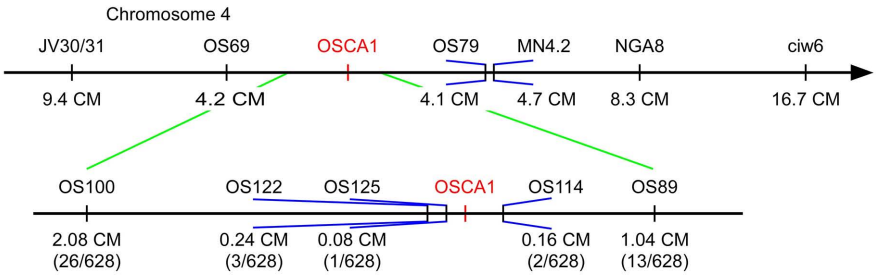

c

Marker name	Physical position (bp)	Primers (forward, reverse)	Type	Restriction enzyme
OS69	1112860	ATTCGGTATCAATGCCTTTC, GATGGAGAAGTTTTACTCTTTTGA	SSLP	
OS100	1344258	CCACGGCACCTGCTAAA, TATACCTGATACTCTTGTTACCCTC	CAPS	ApoI
OS122	1977783	ATTTACAAACCCGAGCCT, TATCTATCACATCCATTACCGT	CAPS	BspCNI
OS125	2098811	CTTTTAATTGTGTATATATAGGATCTTTC, TTATCTTAGACATGCACAATAAAACT	dCAPS	DpnI
OS114	2189910	CTACTATGGATGAGGACGACA, GTTGAAGGCGGGATTGA	CAPS	XmnI
OS89	2378036	TCTCTTCAAACCTCGATCTAAGT, TCTCTTTGTTCATCGTGTGAAT	CAPS	HinfI
OS79	3006988	AACTAATCCAAGTCCAGCACGA, GATAGGGAATGGCATAAGATAAGC	CAPS	MboII

d

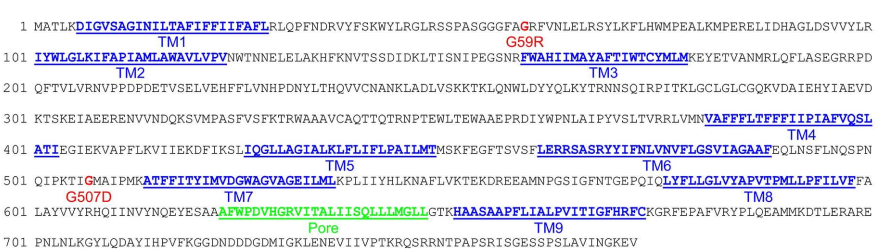

Extended Data Figure 4 | Genetic analysis and map-based cloning of *OSCA1*. **a**, All F_1 seedlings derived from *osca1* × wild-type (WT; ColAQ, Col-0 expressing aequorin) crosses showed wild-type OICI signals. F_2 seedlings showed a 3:1 wild-type:*osca1* segregation, suggesting that the *osca1* phenotype resulted from a recessive mutation in a single nuclear gene. Note that it was not feasible to phenotype the F_2 and F_3 populations from crosses between *osca1* × Landsberg erecta (Ler). The F_2 seedlings, which were derived from *osca1* × Wassilewskija (Ws) crosses and also identified as aequorin homozygous, showed a 3:1 wild-type:*osca1* segregation. The same amount of F_2 seeds for each cross were placed in Petri dishes and OICI phenotypes were scored for individual seedlings (mean ± s.e.m.; $n = 4$ and 6 for *osca1* × ColAQ and *osca1* × Ws crosses, respectively). **b**, Physical mapping of *OSCA1*. *OSCA1* was positioned between JV30/31 and MN4.2 markers in the short arm of chromosome 4 close to centromere in a segregating F_2 population derived from the *osca1* × Ws cross. *OSCA1* was fine-mapped to a region between OS114 and OS125 by analysing 1,256 recombinant chromosomes in the F_2 population with molecular markers listed in **c**. We sequenced all open reading frames (ORFs) in this region between these two makers and identified two mutations in an ORF, which corresponded to the gene At4g04340. **c**, Molecular markers developed for fine mapping. At the time when we were fine-mapping *osca1*, the whole-genome sequence for Ws was not available. Thus, we used the 250,000 single-nucleotide polymorphism (SNP) data to develop these markers. **d**, *OSCA1* encodes a protein with transmembrane α-helices. The transmembrane α-helices (TM; blue), the putative ion channel pore-forming domain (green), and mutations of glycine 59 to arginine (G59R) and glycine 507 to aspartic acid (G507D) in red in *osca1* are shown.

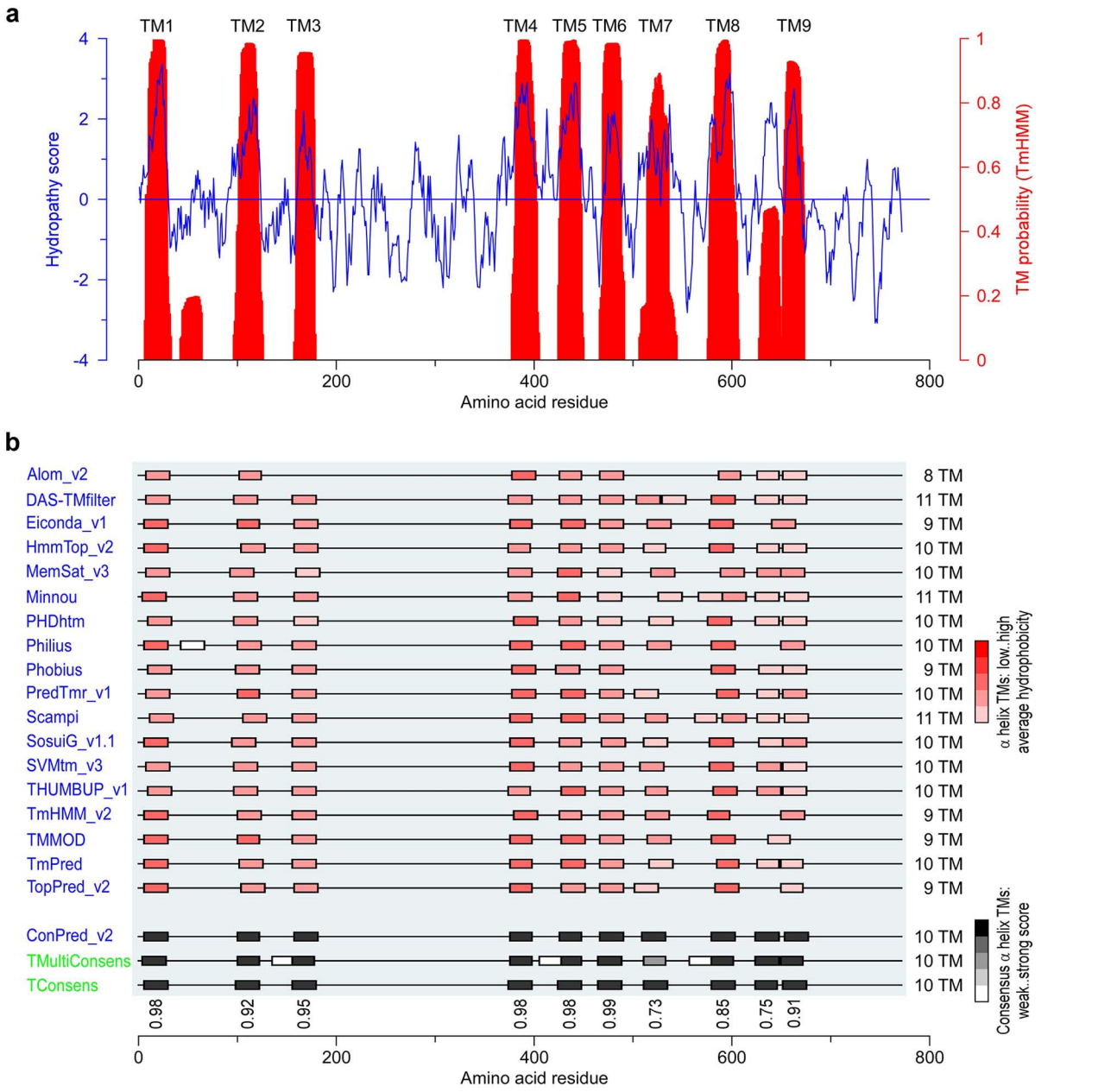

Extended Data Figure 5 | Hydropathy and transmembrane probability plots of OSCA1. **a**, Hydropathy of OSCA1 was calculated using the Kyte–Doolittle algorithm, with a window size of 19 amino acids. The probabilities of transmembrane helices (TM1–TM9) were predicted using TmHMM 2.0 program[59], and the probability plot (red) is superimposed to the hydropathy plot (blue). The region between TM8 and TM9 could be another transmembrane segment (**b**), or a re-entrant pore loop, a common structure in ion channels. Based on the probability prediction, it is most likely to be a re-entrant pore loop, which needs to be verified in the future. **b**, Transmembrane α-helical spanners predicted by Aramemnon (http://aramemnon.botanik.uni-koeln.de)[60].

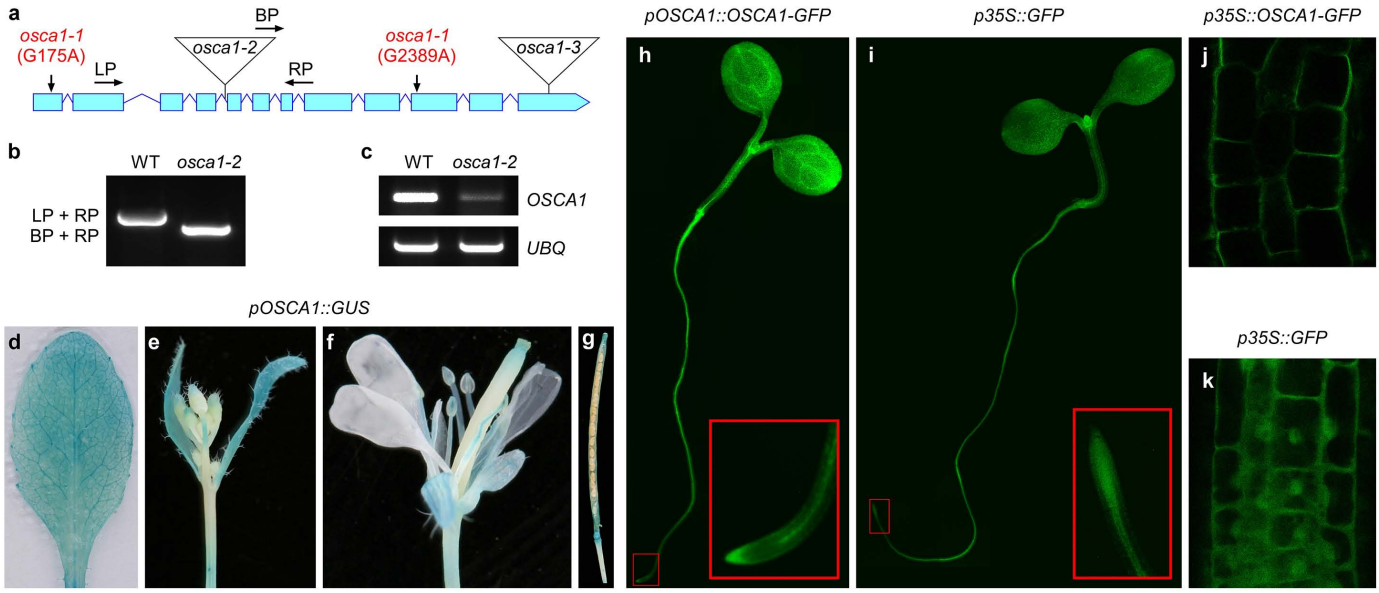

Extended Data Figure 6 | Verification of the T-DNA insertion *osca1-2* mutant and expression patterns and subcellular locations of OSCA1. **a**–**c**, Schematic illustration of the exon–intron structure of *OSCA1* with the boxes representing exons (**a**). The mutations in *osca1-1* and T-DNA insertion sites in *osca1-2* and *osca1-3* are illustrated. Primers for genotyping T-DNA insertion in *osca1-2* are shown. BP, T-DNA boarder primer; LP, *OSCA1* left primer; RP, *OSCA1* right primer. The *osca1* refers to *osca1-1* in this study. Genotyping of an *osca1-2* homozygous line (**b**). PCR reactions with DNA show a flanking DNA fragment upstream (LP) and downstream of the insertion site (RP) in wild type (WT) but not in *osca1-2*, and a DNA fragment flanking the T-DNA boarder (BP) and the downstream of the insertion site (RP) in *osca1-2* but not wild type, suggesting that *osca1-2* is a homozygous T-DNA insertion line. The OSCA1 mRNA level was greatly reduced in *osca1-2*, but the expression of OSCA1 was not abolished (**c**), suggesting that *osca1-2* is a knock-down mutant rather than a null mutant. **d**–**g**, Expression patterns of the *pOSCA1::GUS* in *Arabidopsis* leaf (**d**), flower bud (**e**), flower (**f**) and silique (**g**). The intensity of blue represents the level of GUS activity. **h**–**k**, Expression patterns of OSCA1–GFP in *Arabidopsis* seedlings stably expressing OSCA1 promoter-driven OSCA1–GFP construct (*pOSCA1::OSCA1-GFP*) (**h**) or CaMV 35S promoter-driven GFP construct (*p35S::GFP*) (**i**). GFP fluorescence was analysed using a Zeiss stereo microscope, and images were merged to generate the whole-seedling images. Insets are enlargements of root tips. Over 10 homozygous single-insertion transgenic lines were generated for each construct, and similar results were observed from these lines. Plasma membrane localization of OSCA1 in *Arabidopsis* seedlings stably expressing CaMV 35S promoter-driven OSCA1–GFP construct (*p35S::OSCA1-GFP*) (**j**) or GFP alone as a control (*p35S::GFP*) (**k**). GFP fluorescence was analysed using confocal microscopy. Similar results were seen from over 10 independent homozygous single insertion transgenic lines. In addition, OSCA1 is also predicted to be localized to the plasma membrane by SUBA3 (http://suba.plantenergy.uwa.edu.au/)[18]. Moreover, OSCA1 has been identified independently by several studies of plasma membrane proteomes[19,20,47,61].

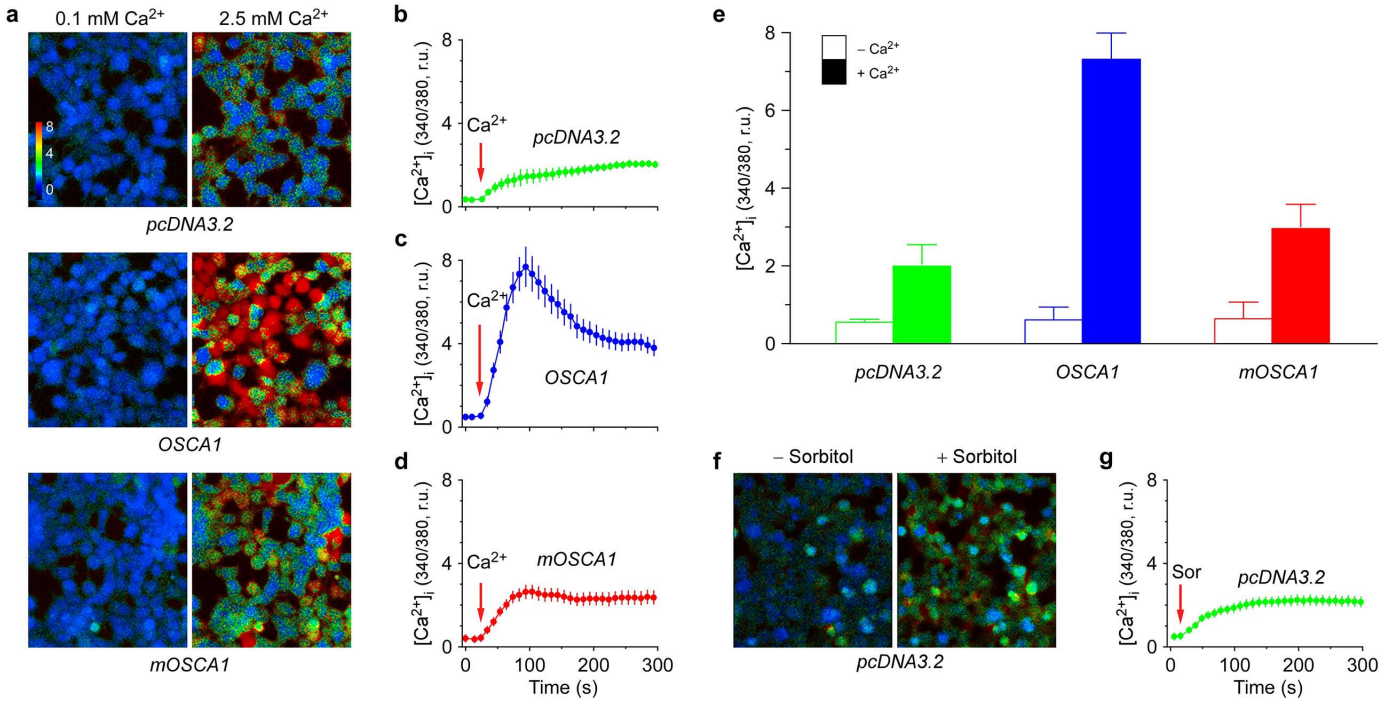

Extended Data Figure 7 | OSCA1 confers calcium-induced $[Ca^{2+}]_i$ increases (CICI) in HEK293 cells. **a**, The increases in $[Ca^{2+}]_i$ in response to elevated Ca^{2+} in HEK293 cells expressing empty vector (pcDNA3.2; top), OSCA1 (middle), or mutant OSCA1 (OSCA1(G59R/G507D) (mOSCA1); bottom). HEK293 cells transiently transfected with empty vector pcDNA3.2, OSCA1, or mOSCA1 were incubated in 0.1 mM Ca^{2+} bath solution, and then treated with 2.5 mM Ca^{2+}. The $[Ca^{2+}]_i$ increase was analysed by Fura-2 emission ratios (F340 nm:F380 nm) and scaled using a pseudo-colour bar. **b**–**d**, Dynamic analysis of CICI in HEK293 cells expressing empty vector (**b**), OSCA1 (**c**) or mOSCA1 (**d**) from experiments as in **a**. Data are mean ± s.d. ($n = 60$ cells; r.u., relative unit). Arrows indicate the time of Ca^{2+} addition. **e**, Quantitative analysis of the peaks of CICI from 80 to 90 s after addition of Ca^{2+} from experiments as in **b**–**d**. We have also carried out experiments with a range of concentrations of Ca^{2+}, and calculated the K_d as 3.6 ± 0.25 mM. Data for three separate experiments are shown (mean ± s.e.m.). **f**, **g**, The $[Ca^{2+}]_i$ increases in response to osmotic stress treatment in HEK293 cells expressing pcDNA3.2, which were used as a control for HEK293 cells expressing OSCA1 or mOSCA1 as shown in Fig. 4a. The cells were incubated in the standard bath solution, and then treated with 650 mM sorbitol. The $[Ca^{2+}]_i$ increases were analysed by Fura-2 emission ratios (**f**). OICIs in HEK293 cells expressing empty vector from experiments as in **f** were quantified (**g**; mean ± s.d.; $n = 60$ cells). Sor, sorbitol.

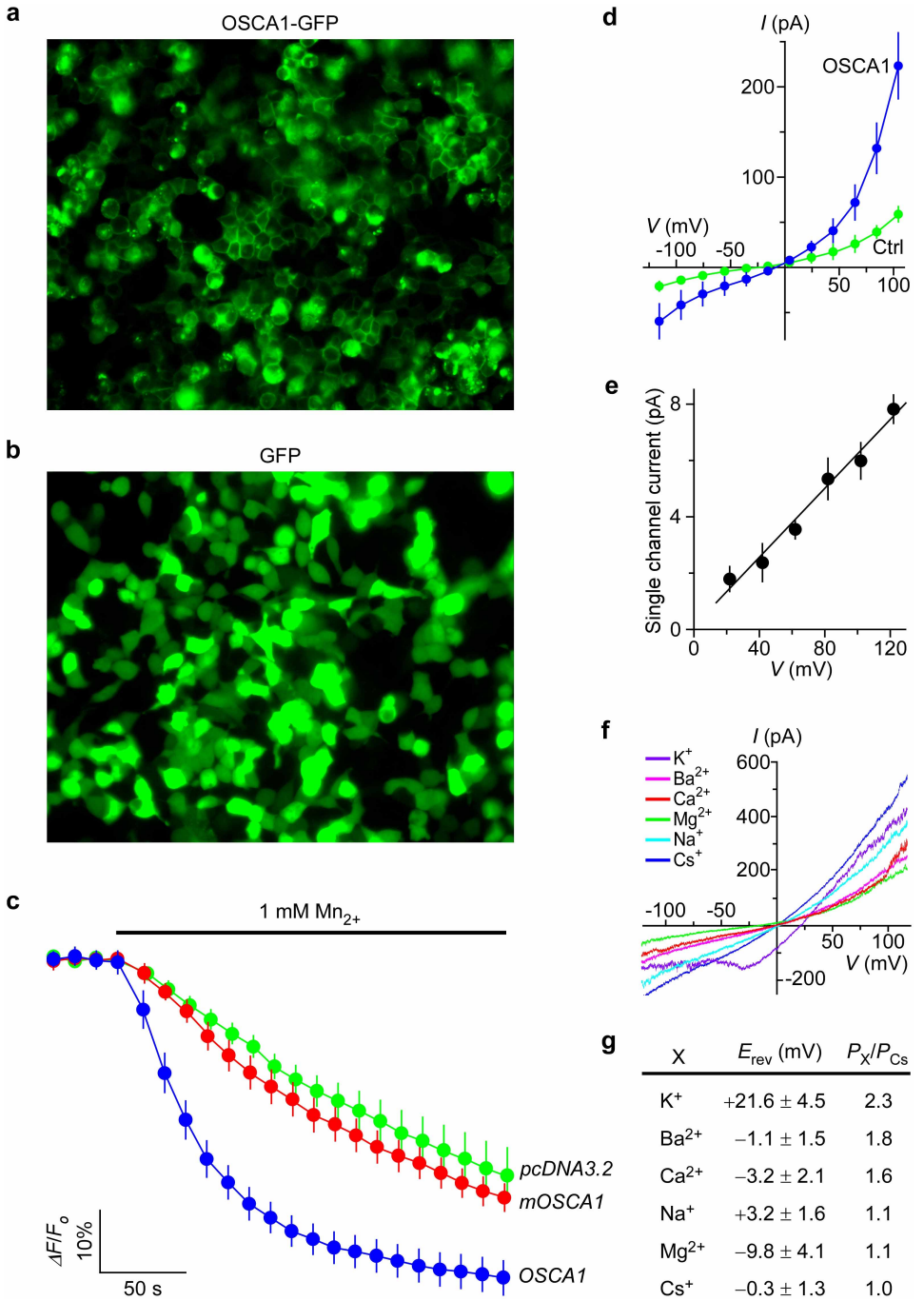

X	E_{rev} (mV)	P_X/P_{Cs}
K^+	+21.6 ± 4.5	2.3
Ba^{2+}	−1.1 ± 1.5	1.8
Ca^{2+}	−3.2 ± 2.1	1.6
Na^+	+3.2 ± 1.6	1.1
Mg^{2+}	−9.8 ± 4.1	1.1
Cs^+	−0.3 ± 1.3	1.0

Extended Data Figure 8 | OSCA1 is localized to the plasma membrane and forms non-selective cation channels with permeability to Ca^{2+} in HEK293 cells. **a**, **b**, HEK293 cells were transiently transfected by OSCA1–GFP or GFP constructs, and GFP fluorescence was analysed using the Zeiss Axiovert 200 fluorescence microscope. OSCA1 was localized in the vicinity of the plasma membrane (**a**); while GFP alone was localized throughout the cells (**b**). These cells were further analysed by confocal microscopy imaging (Fig. 4e). **c**, Ca^{2+} influx across the plasma membrane was analysed using Mn^{2+} quenching of Fura-2 fluorescence in HEK293 cells. HEK293 cells transfected with pcDNA3.2, OSCA1 or mOSCA1 were loaded with Fura-2 and incubated in the standard bath solution. The bath was perfused with the same solution added with 1 mM Mn^{2+}, and quenching of Fura-2 fluorescence at 358 nm was monitored. Percentages show the relative quenching (F, Fura-2 fluorescence intensity F358; F_0, F358 at time zero; mean ± s.e.m.; $n = 60$ cells). **d**, Averaged current-–voltage relationships from experiments similar to those in Fig. 4k (mean ± s.e.m.; $n = 6$ for control and 9 for OSCA1), Ctrl, control. **e**, Current–voltage relationship from single-channel recordings in experiments as in Fig. 4l (mean ± s.e.m.; $n = 4$). **f**, Superimposed whole-cell currents recorded during voltage ramps. OSCA1 currents were first recorded in the standard bath solution and then in solutions containing (in mM) 140 CsCl, 140 KCl, 140 NaCl, 112 CaCl2, or 112 $MgCl_2$. **g**, Relative ion permeability (PX/PCs) of OSCA1 channels from experiments similar to those in **f**. Data are mean ± s.e.m. ($n = 3$ to 9).

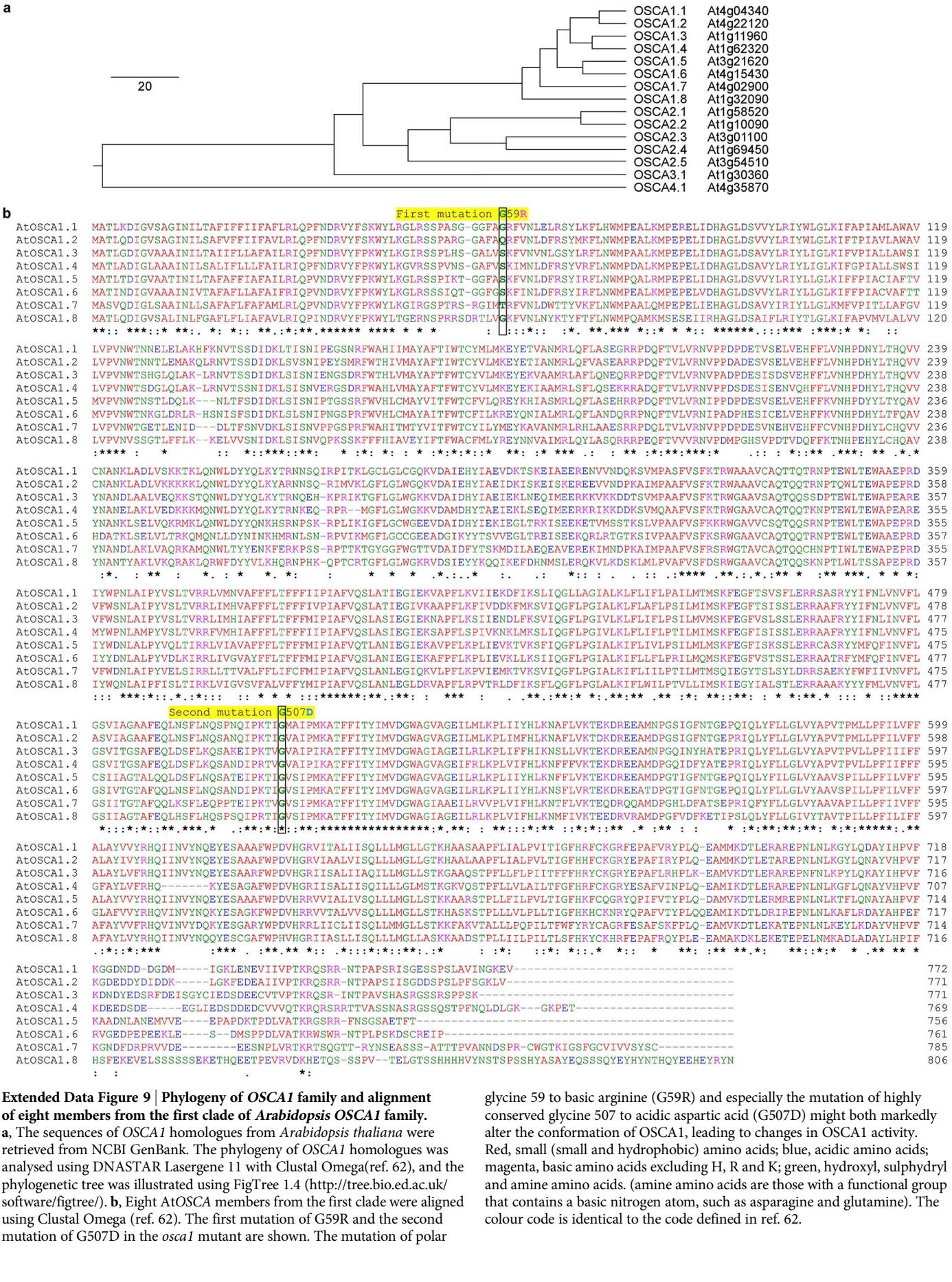

Extended Data Figure 9 | Phylogeny of *OSCA1* family and alignment of eight members from the first clade of *Arabidopsis OSCA1* family. **a**, The sequences of *OSCA1* homologues from *Arabidopsis thaliana* were retrieved from NCBI GenBank. The phylogeny of *OSCA1* homologues was analysed using DNASTAR Lasergene 11 with Clustal Omega(ref. 62), and the phylogenetic tree was illustrated using FigTree 1.4 (http://tree.bio.ed.ac.uk/software/figtree/). **b**, Eight At*OSCA* members from the first clade were aligned using Clustal Omega (ref. 62). The first mutation of G59R and the second mutation of G507D in the *osca1* mutant are shown. The mutation of polar glycine 59 to basic arginine (G59R) and especially the mutation of highly conserved glycine 507 to acidic aspartic acid (G507D) might both markedly alter the conformation of OSCA1, leading to changes in OSCA1 activity. Red, small (small and hydrophobic) amino acids; blue, acidic amino acids; magenta, basic amino acids excluding H, R and K; green, hydroxyl, sulphydryl and amine amino acids. (amine amino acids are those with a functional group that contains a basic nitrogen atom, such as asparagine and glutamine). The colour code is identical to the code defined in ref. 62.

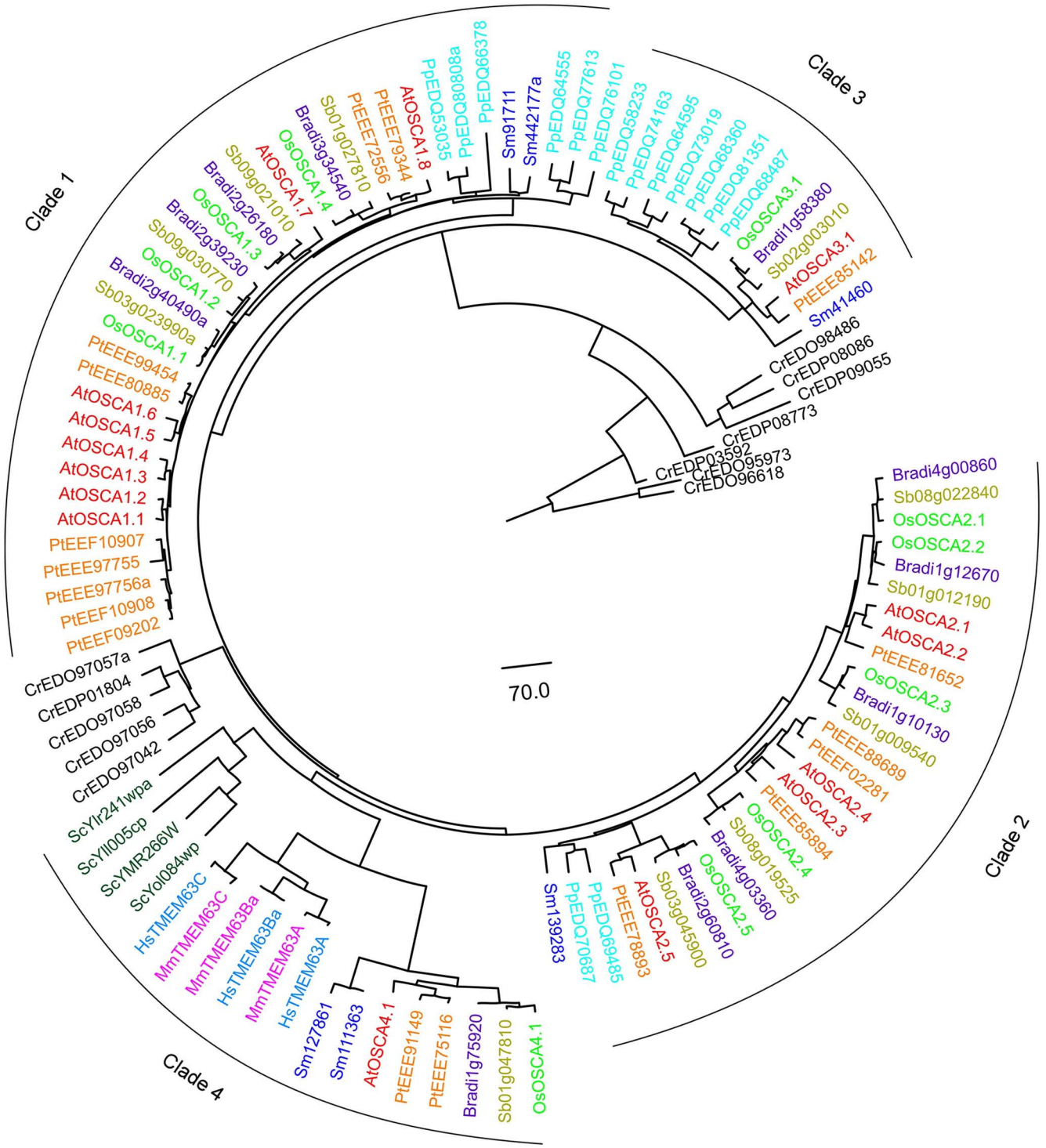

Extended Data Figure 10 | Phylogeny of *OSCA1* family across the taxa. The sequences of *OSCA1* homologues from several species across the taxa were retrieved from NCBI GenBank. The phylogeny of these homologues were analysed using DNASTAR Lasergene 11 using Clustal Omega (ref. 62), and the phylogenetic tree was illustrated using FigTree 1.4. Four clades were classified based on the phylogenetic tree with the clade 3 and 4 uniquely having 1 or 2 genes for vascular plants. At, *Arabidopsis thaliana*; Bradi, *Brachypodium distachyon*; Cr, *Chlamydomonas reinhardtii*; Hs, *Homo sapiens*; Mm, *Mus musculus*; Os, *Oryza sativa*; Pp, *Physcomitrella patens*; Pt, *Populus trichocarpa*; Sb, *Sorghum bicolor*; Sc, *Saccharomyces cerevisiae*; and Sm, *Selaginella moellendorffii*. Os*OSCA1.1*, Os01g0534900; Os*OSCA1.2*, Os05g0594700; Os*OSCA1.3*, Os05g0393800; Os*OSCA1.4*, Os10g0579100; Os*OSCA2.1*, Os12g0633600; Os*OSCA2.2*, Os03g0673800; Os*OSCA2.3*, Os03g0726300; Os*OSCA2.4*, Os12g0582800; Os*OSCA2.5*, Os01g0950900; Os*OSCA3.1*, Os07g0150100; Os*OSCA4.1*, Os03g0137400.

CORRIGENDUM

doi:10.1038/nature14305

Corrigendum: OSCA1 mediates osmotic-stress-evoked Ca^{2+} increases vital for osmosensing in *Arabidopsis*

Fang Yuan, Huimin Yang, Yan Xue, Dongdong Kong, Rui Ye, Chijun Li, Jingyuan Zhang, Lynn Theprungsirikul, Tayler Shrift, Bryan Krichilsky, Douglas M. Johnson, Gary B. Swift, Yikun He, James N. Siedow & Zhen-Ming Pei

Nature **514,** 367–371 (2014); doi:10.1038/nature13593

While we were working on this Letter, Hou *et al.*[1] reported the cloning of AtCSC1, an osmosensitive calcium permeable cation channel. AtCSC1 is a close homologue of OSCA1, which we identified and characterized via forward genetic screens. Whether AtCSC1 functions as an osmosensitive channel in the plasma membrane or endomembranes *in planta* as well as its physiological functions remains to be determined.

1. Hou, C. *et al.* DUF221 proteins are a family of osmosensitive calcium-permeable cation channels conserved across eukaryotes. *Cell Res.* **24,** 632–635 (2014).